Applied Thermal Engineering 205 (2022) 117932

Contents lists available at ScienceDirect

Applied Thermal Engineering

journal homepage: www.elsevier.com/locate/ate

Research paper

The multiscale boiling investigation on-board the International Space Station: An overview

A. Sielaff [a,*], D. Mangini [b,1], O. Kabov [c], M.Q. Raza [d], A.I. Garivalis [e], M. Zupančič [f], S. Dehaeck [g], S. Evgenidis [h], C. Jacobs [i], D. Van Hoof [i], O. Oikonomidou [h], X. Zabulis [j], P. Karamaounas [j], A. Bender [a], F. Ronshin [c,k], M. Schinnerl [a], J. Sebilleau [d], C. Colin [d], P. Di Marco [e], T. Karapantsios [h], I. Golobič [f], A. Rednikov [g], P. Colinet [g], P. Stephan [a], L. Tadrist [k]

[a] Institute for Technical Thermodynamics, Technische Universität Darmstadt, Alarich-Weiss-Str. 10, 64287 Darmstadt, Germany
[b] cosine measurement systems B.V., Oosteinde 36, 2361 HE Warmond, The Netherlands
[c] Kutateladze Institute of Thermophysics, Lavrentyev Prospekt, 1, Novosibirsk, 630090, Russia
[d] Université de Toulouse, Institut de Mécanique des Fluides de Toulouse (IMFT), 2 Allée du Professeur Camille Soula, 31400 Toulouse, France
[e] University of Pisa, DESTEC, Largo Lucio Lazzarino 1, 56122 PISA, Italy
[f] University of Ljubljana, Faculty of Mechanical Engineering, Askerceva 6, SI-1000, Ljubljana, Slovenia
[g] Université libre de Bruxelles, TIPs Laboratory, CP 165/67, Av. F.D. Roosevelt 50, 1050 Brussels, Belgium
[h] Department of Chemical Technology and Industrial Chemistry, Faculty of Chemistry, Aristotle University, University Box 116, 541 24 Thessaloniki, Greece
[i] Belgian User Support and Operations Centre (B.USOC), Ringlaan 3, 1180 Brussels, Belgium
[j] Institute of Computer Science, Foundation for Research and Technology, Hellas, N. Plastira 100 Vassilika Vouton, 700 13, Heraklion, Crete, Greece
[k] Aix Marseille Université, CNRS, Laboratoire IUSTI, UMR 7343, 13453 Marseille, France

ARTICLE INFO

Keywords:
Multiscale boiling
Shear flow
Electric field
Pool boiling
International space station
Microgravity

ABSTRACT

This publication lays the foundation for the description of the Multiscale Boiling Experiment, which was conducted within two measurement campaigns on the International Space Station between 2019 and 2021. The experiment addresses fundamental questions about two-phase heat transfer during boiling processes. For this purpose, single or few subsequential bubbles are selectively ignited on a heated substrate using a short laser pulse. A detailed investigation of the phenomena is possible, as the boiling process is temporally slowed down and spatially enlarged in microgravity. Within the Multiscale Boiling Project, the undisturbed growth of the bubbles, the influence of a shear flow, and the influence of an electric field are investigated within the same test facility using FC-72 as working fluid. Within the project, thirteen research groups from eight countries are collaborating. Over 3000 data sets have been generated over an 11-month measurement period. In the context of this publication, besides the motivation and necessity of such investigations, the basic structure of the experiment, the objectives of the investigations, and the organization are described. Finally, first results of the investigations are presented. Therefore, this publication has the primary aim to serve as a basis for many further planned publications and present the project as a whole.

1. Introduction and motivation

Boiling is a process used in many engineering fields such as energy conversion, environmental applications, food and chemical process industries, and the space sector. It is also encountered in the natural environment, such as geothermal water, geysers, and volcanoes. As a result, there is a great diversity of situations in which boiling processes are present and must be well understood and better controlled. Pioneering work in the field of boiling goes back to Nukiyama's work in 1934 [1]. Nukiyama initially proposed the boiling curve. This curve characterizes the heat transmitted from the heated wall to the boiling liquid as a function of the wall superheat and allows the link between the heat transfer and the boiling regimes. Since then, a huge number of publications were proposed in literature. The majority of the studies are experimental, having an empirical character because of the complexity of the mechanisms. These are, next to others, the heat transfer coupling, nucleation, bubble dynamics, natural convection, evaporation, quenching, condensation, contact line dynamics, wettability, thermocapillary,

* Corresponding author.
E-mail address: sielaff@ttd.tu-darmstadt.de (A. Sielaff).
[1] Former: HE Space Operations BV, Huygensstraat 44, 2201 DK, Noordwijk, The Netherlands.

https://doi.org/10.1016/j.applthermaleng.2021.117932
Received 31 August 2021; Received in revised form 23 November 2021; Accepted 8 December 2021
Available online 1 January 2022

Nomenclature

Symbols

a	thermal diffusivity ($m^2\,s^{-1}$)
C	curve
cg	center of gravity
c	constant
d	diameter (m)
E	electric field intensity ($V\,m^{-1}$)
Q	flow rate ($mL\,min^{-1}$)
F	force (N)
g	gravity ($m\,s^{-2}$)
Δh_v	heat of evaporation ($J\,kg^{-1}\,K^{-1}$)
h	height (m)
I	image
k	thermal conductivity ($W\,m^{-1}\,K^{-1}$)
Nu	Nusselt number
p	pressure (bar)
Pr	Prandtl number
$\dot{q}$	heat flux ($W\,m^{-2}$)
r	radius (m)
R_a	roughness average (μm)
R_z	mean roughness depth (μm)
T	temperature (K)
t	time (s)
U	voltage (V)
V	volume (m^3)

Greek Symbols

α	heat transfer coefficient ($W\,m^{-2}\,K^{-1}$)
β	contact angle (°)
ρ	density ($kg\,m^{-3}$)
σ	surface tension ($N\,m^{-1}$)

Subscripts

ap	apex
b	bubble
bf	bubble foot
dep	departure
elec	electrode
eq	equivalent
gr	growth rate
l	liquid
L	left
lp	laser pulse
mtcr	micro thermocouple rack
on	switching on
off	switching off
R	right
sat	saturation
sub	subcooling
set	set point
v	vapor
w	wall
wait	waiting time
x	x-direction
y	y-direction

and nonequilibrium effects. In most cases, the authors provide characteristic curves of the heat transfer and correlations for applications such as the design of evaporators, steam generators, thermosiphons, and heat pumps. Among these studies, several authors have proposed correlations for evaluating the heat flux density based on the thermo-physical properties of the fluid and the wall (see, for example, Forster and Zuber [2], Forster and Greif [3], Kutateladze [4], Rohsenow [5], Han and Griffith [6], Cooper [7], Stephan and Abdelsalam [8], Gorenflo [9]). The correlations for the evaluation of the heat transfer coefficient, as a function of fluid properties, heat flux, and wall properties, are mostly valid only in the same range of parameters. Dhir [10] emphasized that the correlations' usefulness diminishes very rapidly as parameters of interest start to fall outside the range of physical parameters, for which the correlations are developed. An extrapolation of these relations is not possible or is subjected to significant uncertainties. The massive number of physical phenomena governing the heat and mass transfer process restricts these equations' usability. Two of the most well-known equations for predicting heat transfer can be considered as examples. While the Stephan–Preußer [11] equation (see Eq. (1)) calculates the heat transfer directly from material and process parameters, the Gorenflo equation [9] uses a comparison value estimating the corresponding influences of changing properties (such as for heat flux or pressure). It is also noticeable that the Gorenflo equation does not include the influence of gravity. The Stephan–Preußer equation does not consider the heater material and its shape, which is of great importance for Gorenflo. Despite the effects not considered in the corresponding equations, the already large number of influencing factors underlines the complexity in the prediction and description of boiling processes. Therefore, any study permitting to isolate each factor as much as possible and to look at it from a fundamental point of view would be of great value.

$$Nu = 0.0871 \left(\frac{\dot{q}\, d_b}{k_l\, T_{sat}}\right)^{0.674} \left(\frac{\rho_v}{\rho_l}\right)^{0.156} \left(\frac{\Delta h_v {d_b}^2}{{a_l}^2}\right)^{0.371} \times \left(\frac{{a_l}^2 \rho_l}{\sigma d_b}\right)^{0.350} Pr_l^{-0.162} \tag{1}$$

$$Nu = \frac{\alpha d_b}{k_l} \tag{2}$$

$$\alpha = \frac{\dot{q}}{\left(T_w - T_{sat}\right)} \tag{3}$$

$$d_b = 0.0149\,\beta \left(\frac{2\sigma}{g\left(\rho_l - \rho_v\right)}\right)^{0.5} \tag{4}$$

In Eq. (1), Nu is the Nusselt number defined in Eq. (2), α the heat transfer coefficient defined in Eq. (3), $\dot{q}$ the heat flux density, d_b the bubble departure diameter defined in Eq. (4), k_l the liquid thermal conductivity, T_{sat} the saturation temperature, T_w the wall temperature, ρ_v and ρ_l the vapor and liquid densities, respectively, σ the surface tension, g gravitational acceleration, Δh_v the heat of evaporation, a_l the liquid thermal diffusivity, Pr_l the liquid Prandtl number, and β the contact angle in degree.

1.1. Boiling in microgravity

As stated in the previous section, the physics of the boiling process is still poorly understood because of the complexity of the phenomena involved. At first glance, one might therefore assume that the primary purpose of boiling studies in microgravity would be building correlations for future space applications like cryogenic fuel storage, propulsion, life support systems, and cooling systems, comparable to

the correlations experimentally investigated under earth gravity. A simple comparison shows that these existing equations are not suitable for reduced gravity (beyond their previously described limitations). If one changes the gravity in the two equations mentioned above with respect to any reference value, the Gorenflo equation shows no influence of gravity at all. The Stephan–Preußer equation shows a $\alpha \propto g^{-0.101}$ relationship, while the correlation of Raj et al. [12], developed especially for variable gravity, shows a $\alpha \propto g^{0.196}$ relationship (for a nondimensional wall temperature of 0.5), having a completely different trend.

The creation of such correlations is a pronounced goal, especially regarding later technical applications. However, on more detailed consideration, the experimental investigation of boiling processes under microgravity offers far greater potential. A microgravity environment can allow a better comprehension of the underlying phenomena in the boiling process. Gravity tends indeed to make the understanding of the boiling process extremely complex for several reasons. First of all, the thermally-driven buoyancy flows overshadow other important physical phenomena such as thermo-capillary flows, bubble-induced convection, and transient thermal diffusion, to cite a few. Such phenomena are not only surpassed by the thermally driven buoyancy flows, but they are also intrinsically coupled with them. Such a coupling effect is highly non-linear. As such, the unique possibility of a better comprehension of all the physical phenomena that are masked by gravity is only possible if the overall physical process is studied and analyzed in microgravity. Moreover, considering that the gas and liquid densities differ by several orders of magnitude, hydrostatic stresses cause vertically-orientated forces. The vapor/liquid interface can also be distorted if the hydrostatic pressure gradients are comparable or exceed surface tension stresses. Microgravity thus can clarify the evaluation and the understanding of natural stresses (e.g., static pressure, capillarity), and/or imposed stresses (e.g., shear, electrostatic) on the boiling process. Moreover, microgravity tends to slow down and enlarge phenomenological events. When gravity dominates, the bubble departure and interface instabilities tend to occur at time and length scales that strain the capabilities of scientific measurement equipment. A microgravity environment exposes boiling phenomena in such a way that facilitates higher temporal and spatial resolution, offering more in-depth insight into underlying physics.

Next to the design of two-phase heat transfer systems for space applications, the scientific potential of investigating boiling processes in microgravity led to the start of such investigations as soon as the technical conditions were met. Most of the low gravity experiments were initiated using ground-based facilities like drop towers (e.g., [13]). Since the end of the 1980s, next to drop tower experiments, experiments were carried out using short-duration microgravity facilities like parabolic flights (e.g., [14–18]), and sounding rockets (e.g., [19–21]). In the 90's, the shuttle was used to perform experiments [22,23]. Further research had been performed within a SJ-8 [24] or Foton [25] satellite. In addition, two pool boiling and one flow boiling experiment could already be carried out on-board the International Space Station (ISS) [26–28]. All previous space experiments have already demonstrated a significant influence of gravity on the boiling process. In spite of the great potential, the study of boiling processes in microgravity also brings particular technical challenges. In order to be able to investigate the phenomena mentioned above in the best possible way, a single bubble or several bubbles should be able to grow as undisturbed as possible in a defined far field. In addition, a measurement technique with a high spatial and temporal resolution is necessary. For the performance of several successive experiments, it is necessary to remove the bubbles from the experimental area or to recondense them. Furthermore, especially in microgravity, disturbances can also occur due to uncontrolled nucleation and subsequent coalescence of several bubbles. Hence, this has to be controlled by the chosen experimental setup. For more extended test periods, it is also necessary to remove the bubbles from the heating surface during the test, since otherwise the complete test area will be covered with vapor after a particular time, which will lead to a significant influence of the heater size, geometry, and experimentation time on the heat transfer [27]. The implementation and the realization of the described conditions are primarily influenced and limited by the chosen test platform. Therefore, the available platforms will be briefly discussed in the following.

1.2. Microgravity platforms: The International Space Station as a research tool for pool boiling experiments

Several platforms are currently available to carry out experiments in weightlessness, or reduced gravity [29]. Common to all platforms is that an experimental container is exposed to a free fall for a given time. Next to others, this free fall can be achieved in a drop tower, a parabolic flight, a rocket, various satellites, or installing the experiment onboard the International Space Station. However, the platforms differ significantly in the experiment's permissible size, the accessibility during the investigation, possible data transfer, the duration of microgravity, and its quality. In Fig. 2 the different platforms are compared in terms of microgravity quality and duration. One of the most common platforms is a drop tower. For example, the ZARM at the University of Bremen (Germany) has a drop tower with a height of about 120 m, from which a capsule with an experimental setup is dropped. To increase the duration of the experiments, a catapult that shoots the capsule upwards can be used. In this case, the duration of microgravity is up to 9.2 s. Another ground-based platform used for performing tests at different gravity levels is a parabolic flight. As in the drop tower, the experimental setup is in free fall. One parabolic maneuver lasts about one minute. During the parabolic maneuver, the acceleration value changes from normal to increased (1.8 g to 2 g) for about 20 s, then microgravity (1×10^{-2} g) sets in for approximately 20 s, after that, within 20 s, the flight takes place at an increased acceleration value (1.8 g to 2 g) to recover to normal flight. A unique feature of this platform is that the scientists are in the aircraft at the same time and can directly interact with the experiment. In addition, all gravity levels between 0 g to 1 g can be set, extending the reduced gravity duration. Sounding rockets represent another possible platform for performing tests in microgravity, allowing up to 13 consecutive minutes of microgravity (MAXUS type Sounding Rocket). Commands are sent to the equipment located inside the rocket directly during the experiment. The residual acceleration in microgravity is less than 1×10^{-4} g. Satellites and shuttles were also used to conduct experiments in microgravity. The experiment duration is generally much longer than for sounding rockets. Other circumstances, such as data transfer, depend highly on the respective mission. Space Stations are high-end platforms for many different experiments. Experiments are carried out on the International Space Station (since 1998) and Mir station (1986–2001). Another space station is planned to be launched in 2021 — the China Large Modular Space Station. The European Space Agency has integrated the research module Columbus within the International Space Station in February 2008 including ready-to-experiment workbenches, like the hydrodynamic research stand (Fluid Science Laboratory — FSL). The residual acceleration measures about 1×10^{-4} g and could even be less depending on the vibrational frequencies [30]. A constant data transfer is possible in both directions, so that even during a campaign the test execution can be influenced based on the prior measurement results. (See Fig. 1).

1.3. Research and publication objectives

The boiling processes to be investigated take place under microgravity for several seconds. Times for setting the process parameters are in the range of several minutes. To cover a sufficient parameter range, microgravity of a long duration is therefore necessary. The required high-resolution measurement techniques will generate a vast amount of data. In order to influence the further course of the measurement based on initial results during the experimental campaign, these data

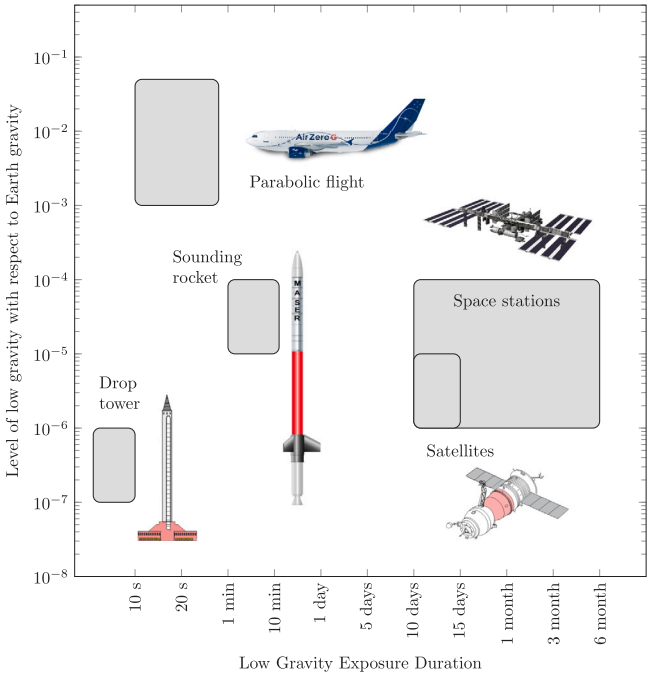

Fig. 1. Comparison of gravity levels (relative to Earth gravity) and their durations for different microgravity platforms.

must be transferred to Earth throughout the campaign, which requires an appropriate communication platform. Finally, the quality of microgravitation must be good enough to exclude any significant interference from the experimental platform. Hence, the International Space Station was chosen as the ideal experimental platform for this project because it fulfills all major requirements mentioned above.

The Multiscale Boiling Experiment investigates a single or a low number of several bubbles under microgravity conditions. A complex diagnostic system, with synchronized infrared (IR) and high-speed black and white (BW) imaging, should lead to a better comprehension of the overall process and is intended to contribute to an authoritative database for the validation of numerical models. The removal of vapor above the heated surface, which is essential for more extended technical use, can be done in microgravity through shear flow or electric field. These techniques will not only be used in this project but will be investigated for the first time under such conditions. Furthermore, a direct comparison to boiling with and without these external forces is possible.

As described in the previous section, many questions remain unanswered despite much previous work on boiling, in normal and microgravity conditions. To contribute to the clarification, the Multiscale Boiling Project (also known as RUBI) has been started in 2005. Supported by several preliminary works in the laboratories of the participating institutions as well as on parabolic flights (e.g. Nejati et al. [31]), Airbus DS could complete the development and setup of the experiment in 2019. Afterward, the experiment was launched towards the ISS on July, 25th 2019, where it became operational on September, 6th 2019.

In this publication, the project will be presented as a whole for the first time. In the following, the detailed objectives of the project, as well as the organization (Section 2), will be presented. The experimental setup, the execution of the experiment, and the evaluation will be described in detail. More detailed descriptions, for example, of the individual evaluations, will be described in dedicated publications in the future, as this would go beyond the scope of a single publication. Section 4 gives a first insight into the scientific results of the project.

2. The multiscale boiling experiment

2.1. Objectives

The objectives of the Multiscale Boiling Project can be divided into six groups. While the first four objectives had been investigated within the described experimental setup, this was unfortunately not possible for objectives five and six due to technical limitations. Therefore, they will not be further discussed. These objectives will be investigated in the future as part of the project.

Objective 1: *Observation of the contact line behavior on single bubbles*

From many previous investigations, it is known that the contact area between the heated surface, vapor, and liquid contributes significantly to the heat transfer during boiling and thus has a significant influence on the process. Due to the slowed growth in weightlessness, micro-scale effects in this area can be investigated in detail. In particular, the wall temperature and its distribution, the contact angle of the bubble, and the heat flux density that is transferred are to be mentioned.

Objective 2: *Observation of individual bubble growth*

During bubble boiling, the applied heat causes the liquid in the superheated area near the wall to evaporate and accumulate in bubbles due to surface tension. Thus, a single bubble represents an elementary cell of boiling. The life cycle of a bubble consists of nucleation, growth rates, and departure. The aim is to investigate the heat and mass transport concerning the individual life phases in more detail. Also, the influences of Marangoni convection and non-condensable gases are to be examined more closely. Nucleation, growth, and departure of a bubble are subject to a wide variety of force influences. The dominant factor of gravity in ground experiments can be eliminated in this investigation. For the observation of single bubbles' growth, the external forces of a shear flow and an electric field are, therefore, in the foreground in this aspect.

Objective 3: *Influence of an electric field*

An electrode placed above the nucleation site is supplied with a high voltage source. A sufficiently strong electric field can affect bubble growth rates, shapes and heat flux densities. Besides, an electric field can also cause a movement or a departure of the entire bubble, making the technology a possible substitute for gravity. In this sub-area, the influences of the electric field must be comprehensively investigated.

Objective 4: *Influence of a Shear flow*

Like with an electric field, an external force can also be applied to a bubble by shear flow. Furthermore, a shear flow has a significant influence on the thermal boundary layer in which a bubble grows. Both effects are also superimposed by the force of gravity in ground experiments. This section aims to investigate significant phenomena between shear flow, thermal boundary layer, and bubble growth.

Objective 5: *Single bubbles in binary mixtures*

The influence of a second or even more components is significant in the boiling process. In the area of the highest heat and mass transfer, a concentration of less volatile components occurs, and thus the material properties at the microscale level show significant differences. This sub-area aims to investigate the influence on heat flow and bubble growth. Since a fluid change is not possible on the International Space Station due to technical limitations, this goal will be achieved by the already mentioned additional parabolic flights and further ground experiments.

Objective 6: *Influence of bubble interaction*

As clarified in Objective 1, a single bubble represents the boiling process' elementary cell. In technical applications, the growth of several bubbles nearby leads to interaction and coalescence, which significantly influence the boiling process and the heat flux density. Thus, this sub-section represents the largest scale range in the presented investigation and the interface to global studies and correlations. A systematic study of bubble coalescence, similarly to the situation in Objective 5, is not explicitly foreseen in the experimental setup due to the technical limitations. However, spontaneous bubble interactions are used, and further studies will be accomplished in the framework of additional laboratory and parabolic flight experiments.

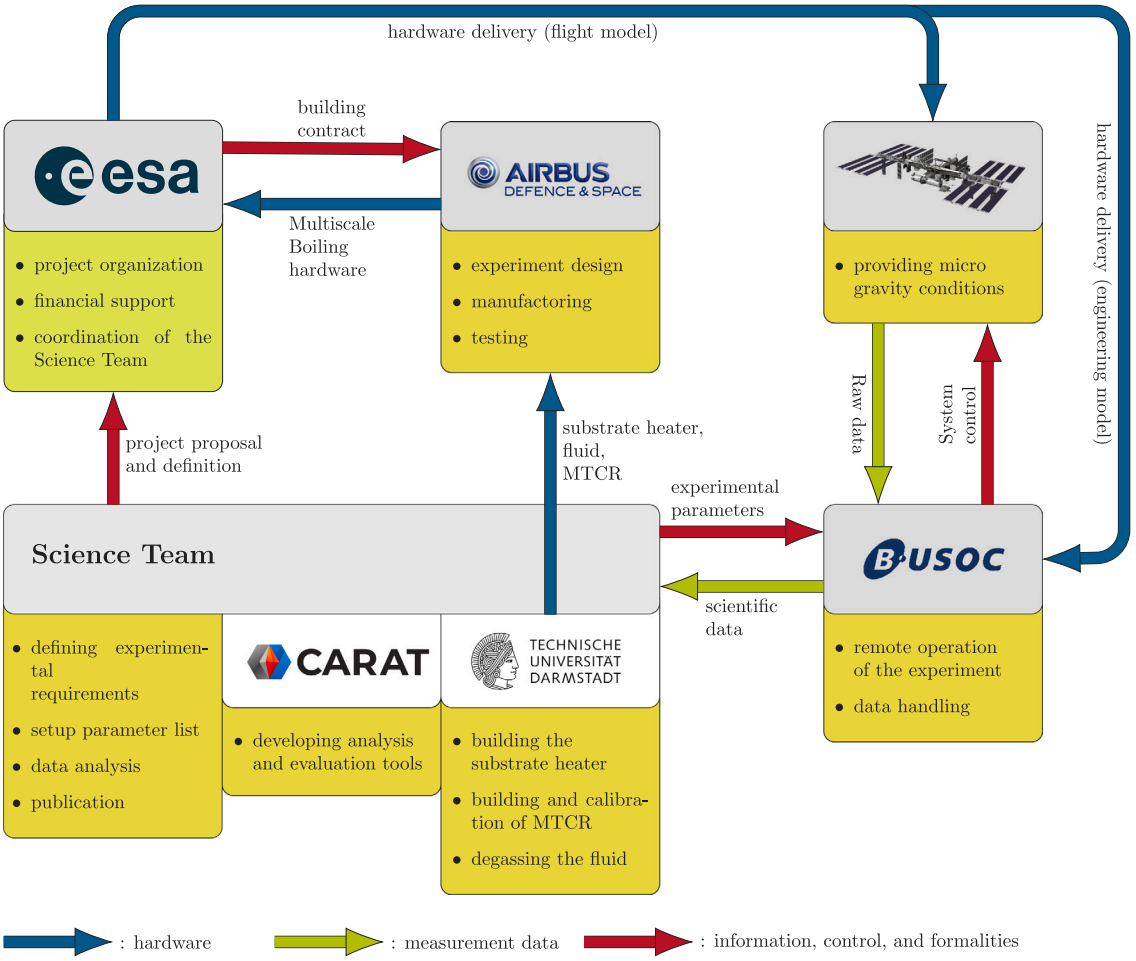

Fig. 2. Organizational structure in the Multiscale Boiling Project.

2.2. Organization

To successfully implement such an ambitious project, good cooperation between different partners is essential. Fig. 2 shows the organizational structure within this project in a simplified form. After the team of scientists developed the idea for this project, a corresponding application for implementation is submitted to the European Space Agency (ESA). After examination and approval, ESA takes over the project organization and provides the necessary financial means. Within the framework of a tender, Airbus Defence and Space was subsequently selected as the industrial partner to build and test the experiment hardware according to the Experimental Scientific Requirements (ESR) defined by the scientists. The heater developed by the TU Darmstadt, which had already been tested in the laboratory and on several parabolic flights, was intended for use onboard the ISS and was therefore provided by the Science Team.

The hardware was designed so as to fit in a so-called experiment container (EC) for the Fluid Science Laboratory (FSL), which is one of the experiment hosting racks in the European Columbus model on the International Space Station. After completing the hardware, the functionality was verified in the Misson Test 1 and the Science Validation Test (SVT) at Airbus. The hardware was handed over to ESA upon the successful completion of these tests. The hardware consisted out of two similar Experiment Containers: one Flight Model (FM) used to conduct the actual experiment in microgravity, and one Engineering Model (EM) used on ground for additional testing, operator training, or in support of anomaly resolution. During the SVT almost 100 experiments were performed on ground with the FM, to compare results achieved with the same hardware at different g-levels. The on-orbit operation, preparation, and execution were performed by the Belgian User Support and Operations Centre (B.USOC) on behalf of ESA. The Multiscale Boiling hardware FM was sent to the International Space Station on a SpaceX Dragon Capsule (SpaceX CRS-18 mission) and installed by the ESA astronaut Luca Parmitano on August, 9th 2019 in the FSL in the Columbus module of the ISS (see Fig. 3). Once the hardware is installed, the entire experiment can be controlled from ground without the intervention of an astronaut. The B.USOC executed the Multiscale Boiling experiment runs based on the parameters defined by the Science Team after commissioning and further testing. The data collected was then converted into readable formats and made available to the scientists for further analysis. The CARAT group was founded to unify the algorithms for evaluation and analysis and to evaluate the massive amounts of data efficiently. Within this group, the corresponding tools are collaboratively created, extended, and validated. They are available to the whole team.

3. Experimental setup, on-orbit calibration, and test execution

3.1. Experimental setup

To achieve the objectives presented in Section 2.1, the experimental setup sketched in Fig. 4 was designed and built. The working fluid is

Fig. 3. Luca Parmitano prepares the Multiscale Boiling EC for installation within the FSL.

degassed FC-72 (C_6F_{14}). The test cell consists of an aluminum block thermalized by Peltier elements. In the bottom area of the cell, the infrared transparent heater is installed so that it is leveled with the surrounding cell. The heater consists of a coated barium-fluoride crystal (see Section 3.2). To be able to thermalize the fluid, a preheater and a condenser are used. Both are — like the cell itself — flowed through by a pump. This pump is also used to achieve the objectives shown in Section 2.1, i.e., to apply external forces to a bubble through a shear flow. The flow rate is adjustable and can be controlled by a separate flowmeter. There is a honeycomb in the inlet area of the cell and a flow guide at the inlet and outlet to even out the flow. The use of preheaters and condensers is necessary to adjust the system parameters and protect the pump against cavitation, as the working fluid is used near its saturation point. The size of the cell is designed to measure bubble up to a diameter of 10 mm. The influence of an electric field (see Objective 3) can be examined using the electrode placed centrally above the heater. The electrode has a shape similar to a washer and is continuously adjustable in height between 6 mm to 10 mm (distance from the heater surface). Further, it can be brought to a so-called homing position, fully retracted far away from the heated surface. An additional bellow is included for adjusting the system pressure by increasing or decreasing the system volume accordingly. This makes it easy to investigate different subcoolings at a given fluid temperature. Besides, the bellow is used to condense remaining vapor bubbles after a test by increasing the pressure far above saturation (generally 1.3 bar).

In addition to several pressure and temperature sensors distributed in the setup, and the volume flow sensor mentioned above, the setup contains three primary measuring techniques. A micro thermocouple rack probe (MTCR) consists of four ≤100 µm thick measuring points, to measure the profile of the thermal boundary layer. The MTCR is applied at an angle of 43° (to the boiling surface). The individual measurement points have a distance of 3 mm to each other. Like the electrode, the probe is freely movable in height along its axis with a smallest distance to the heated surface of 0.36 mm (with respect to the lowest of the four measurement tips). For safety reasons, the motion of one actuator is possible solely if the other one is in its homing position. In this way, a possible interference between the MTCR and the electrode is avoided by hardware. The shape of the bubbles is recorded from the side by a black and white high-speed camera. A high-speed infrared camera records the temperature field of the heater at the bottom of the coated layer. From these images, the temporally and spatially resolved heat flux profiles can be calculated (see Section 3.4.2).

Table 1
Operating range and parameters of the experiment.

Test cell		
Pressure (experiments)	500 to 1000	mbar
Pressure (recondensation and thermalization)	500 to 1500	mbar
Temperature	30 to 70	°C
Flow rate	100 to 700	mL min^{-1}
Leakage rate (He)	1.63×10^{-5}	mbar L s^{-1}
Leakage rate (SF6) calculated	2.74×10^{-6}	ppmv/s
Measuring frequency	1	Hz
Heater		
Heat flux	0 to 2	W cm^{-2}
Range with no parasitic nucleation	0 to 1.2	W cm^{-2}
Laser		
Power	177	mW
Pulse duration	0 to 1000	ms
Electrode		
Distance from surface at usage	6 to 10	mm
Voltage	0 to 15	kV
Microthermocouple rack		
Distance from surface at usage	≥ 0.36	mm
Measuring frequency	≤ 10	kHz
High-speed black and white camera		
Used field of view	22.27 × 15.18	mm
Used no. of pixels	1100 × 750	pixel
measuring frequency	≤ 500	Hz
High-speed infrared camera		
Field of view	4.98 × 26.56	mm
No. of pixels	120 × 640	pixel
Measuring wavelength	8 to 14	µm
Measuring frequency	≤ 240	Hz

To create a bubble at a desired time and place, the heater contains a defined cavity in the substrate's middle (see Section 3.2). Secondly, a laser beam is used to overheat the cavity to ignite the first bubble.

A picture of the open experimental container is shown in Fig. 5. In the middle of the picture one can see the boiling cell ① with the electrode above the substrate heater. Above the boiling cell one can see the actuator of the electrode ② and the one of the MTCR ③. Below the boiling cell the infrared camera ④ is mounted, right to the preheater ⑤. On the lower right part the electronics and measurement technique ⑥ can be seen. The black and white camera is located behind the boiling cell and cannot be seen from this perspective.

The operating range of the experiment and relevant operating parameters are shown in Table 1. A very detailed description of the experimental setup and an error estimation is omitted at this point and will be presented in a dedicated future publication.

3.2. Substrate heater

The heater consists of a 5 mm thick barium-fluoride crystal. There is a 2.5 mm chamfer on the upper side, so the surface onto the fluid has a diameter of 20 mm. The crystal is optically transparent in the range of 150 nm to 15 µm wavelength. In the middle of the surface, the crystal contains an L-shaped cavity created by ultrashort pulse laser ablation. The cavity has a diameter of 30 µm and a depth of 200 µm. The lateral length below the surface is 100 µm. The L-shape is chosen to hold a small amount of vapor inside the cavity. Especially for measurements with shear flow and an electric field, when bubble departure is expected, this should enable continuous nucleation on the smooth surface without renewed overheating by the laser. The crystal is first coated with chromium nitride and then with chromium using physical vapor deposition. Both layer thicknesses are about 400 nm. The lower layer (chromium nitride) is used to increase the emissivity to ensure a more accurate temperature measurement with the infrared camera. The upper layer serves primarily as a Joule heater. Besides,

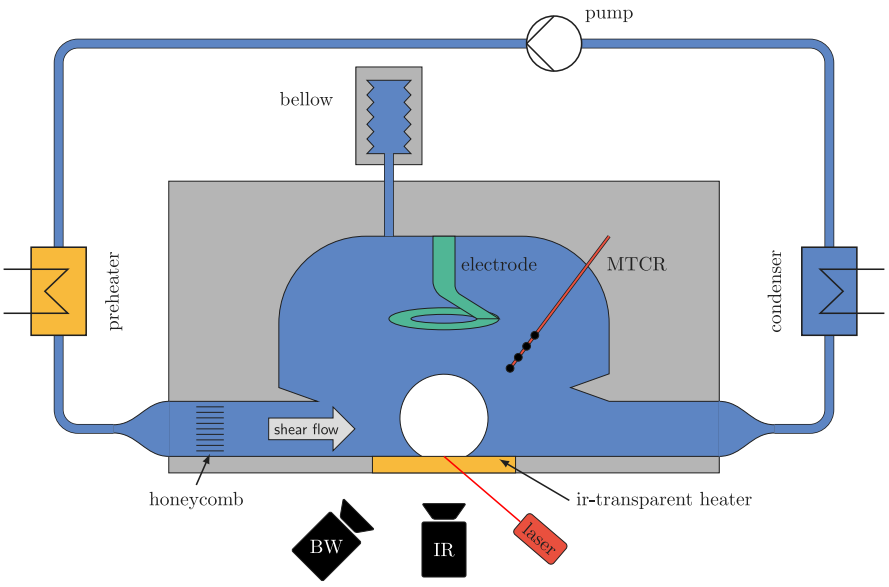

Fig. 4. Schematic of the experimental setup. The black and white camera captures the bubble from the side (image plane of the sketch) with back illumination.

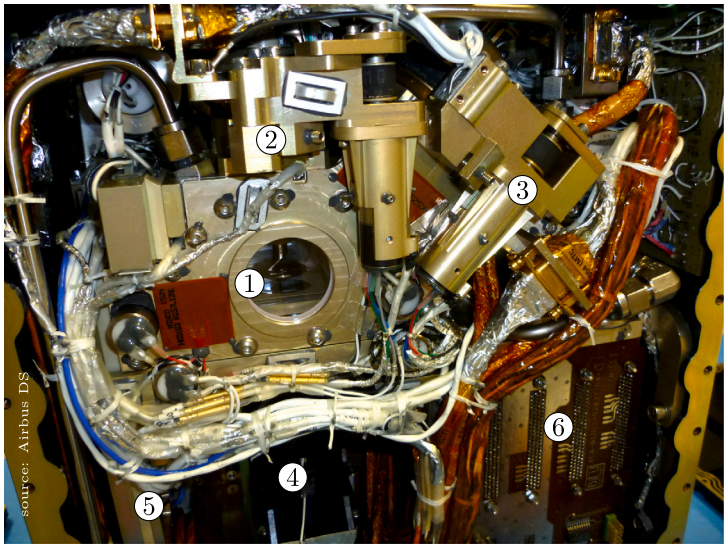

Fig. 5. Picture of the open experimental container. 1: boiling cell with the high voltage electrode above the substrate heater; 2: actuator of the high voltage electrode; 3: actuator of the micro thermocouple rack; 4: infrared camera; 5: preheater; 6: electronics and measurement.

this upper layer increases the overall emissivity of the structure to > 0.9. The surface roughness of the coated heater (with the exception of the cavity) is $R_a < 0.02\,\mu m$ and $R_z < 0.11\,\mu m$ [31]. At the chamfer of the substrate heater, a copper layer is used on each side to reduce the contact resistance and hence avoid parasitic boiling at these positions.

Besides, this layer increases the overall emissivity of the structure to > 0.9. At the chamfer of the substrate heater a copper layer is used on each side to reduce the contact resistance and hence avoid parasitic boiling at these positions.

The coating of the crystal is designed in a tailored form to minimize the probability of parasitic boiling at the edges of the crystal while keeping the heating power in the scientifically interesting area as homogeneous as possible.

To ensure a flat connection to the cell, the crystal is enclosed by a polyetheretherketone (PEEK) cover, which at the same time, transfers the force required to seal the assembly to the crystal. Since the E-modulus of PEEK is too low to provide a flat surface and to apply the necessary force for a sufficient seal, the cover is reinforced with stainless steel rails at the sides. The heater assembly is shown in Fig. 6. As the same setup has already been used in a parabolic flight campaign more details can be found in Nejati et al. [31].

3.3. Test execution

The operations of the first Multiscale Boiling campaign started on September, 6th 2019 and lasted until March 5th 2020. Afterward, a second campaign was performed between October, 15th 2020 and

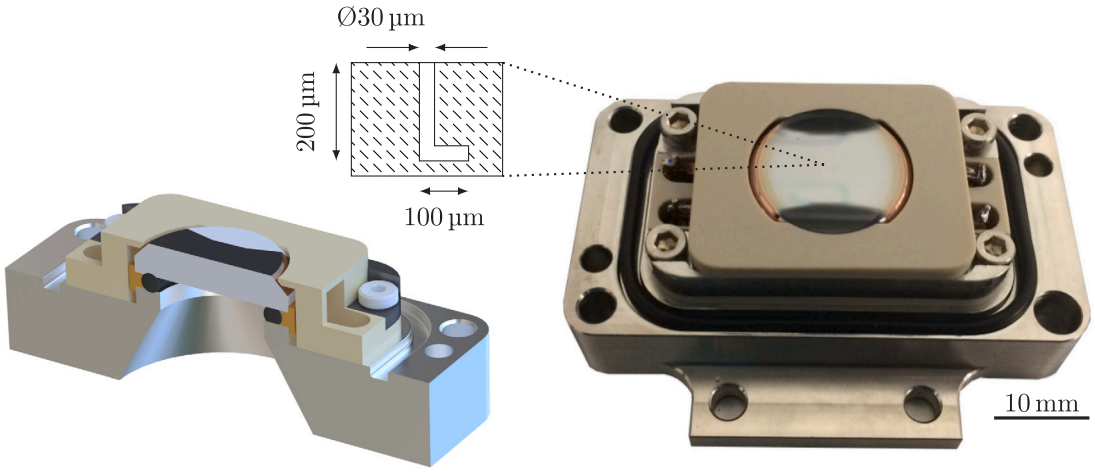

Fig. 6. Assembly of the substrate heater: On the left side without connecting cables. On the right side as picture with an enlargement of the artificial cavity as cut view.

January, 13th 2021. After the initial installation of the hardware and the successful activation, a series of commissioning activities was performed. These included both a functional checkout of the hardware as well as a science commissioning. Part of the functional checkout consisted in collecting a series of reference infrared images at various liquid temperatures, required for the calibration of the high-speed infrared camera. The science commissioning was mainly a repetition of the experiment runs performed during the Science Validation Test campaign on ground. The commissioning activities were successfully completed on September, 23th 2019 and were followed by a science campaign starting on October, 1st 2020. The science runs were monitored and commanded from ground by B.USOC, taking into account the input and requests of the science team. A high level schematic of the end-to-end data flow is presented in Fig. 7. From the experimental container the data are transferred through the Fluid Science Laboratory (FSL) and the Columbus module to the communication system of the ISS. Due to the low altitude of the ISS (approx. 400 km), a permanent direct connection to Earth would only be possible by means of multiple ground stations spread all over the world. Therefore, the signal is transmitted to the ground stations via the Tracking and Data Relay Satellite System (TDRSS) with a geostationary orbit (approx. 40 000 km). NASA sorts the signals and forwards the Columbus Module data to the Columbus Control Center (ColCC) in Oberpfaffenhofen. The ColCC sorts the data according to their affiliation. All data concerning the Multiscale Boiling Experiment is transferred to the B.USOC in Brussels. The B.USOC operators can receive data from the EC as well as send commands to the EC. All participating scientific groups have read-only access via a user home base and can follow the EC data in real time. The duration of the communication is generally less than 1 s for sending a command and receiving the corresponding response by a B.USOC operator.

The execution of the experiment is driven by the Experiment Procedure (EP), a collection of Tool Command Language (TCL) scripts. A custom TCL interpreter residing on the FSL main computer executes the EP. The EP can send commands to the FSL main computer via interface functions and can read telemetry values via a mechanism that links telemetry elements to TCL variables through a monitoring table. The EP can also receive on event telemetry from the EC and FSL subsystems, but also messages from ground. The EP functions can be called directly by dedicated telecommands, or through a text file referred to as parameter table, which allows for the semi-automatic execution of the experiment. The parameter tables are prepared by B.USOC and uplinked to the ISS on regular basis. An experiment is defined by the following parameters: The liquid pressure p_l, the saturation temperature T_{sat}, the subcooling T_{sub}, the heat flux of the substrate heater $\dot{q}$, the electrical voltage applied on the electrode U_{elec}, the flow rate Q, the height of the electrode above the substrate heater h_{elec}, the height of the MTCR above the substrate heater h_{mtcr}, the time between the activation of the substrate heater and the onset of the laser pulse t_{wait}, the duration of the laser pulse t_{lp}.

Concerning the scientific objectives (see Section 2.1) four main categories of experiments are defined within this 10 dimensional parameter space:

- **Pool Boiling:** No flow or electric field is applied. The electrode is at its highest position and the micro-thermocouple rack as close as possible to the substrate heater, i.e. at 0.36 mm above the heater.
- **Shear Flow:** Similar to pool boiling but shear flow is applied.
- **Electric Field:** No flow is applied and the MTCR is at its highest position. The electrode is lowered to a position between 10 mm and 6 mm above the substrate heater.
- **Shear Flow and Electric Field:** Similar to electric field experiments but with active flow.

Fine-tuning. A first phase in the experiment execution was the so-called fine-tuning, where the system characteristics in microgravity are investigated. The liquid cell contains several temperature sensors and auxiliary heaters, which provide a mean to control the temperature of the liquid. Due to the absence of gravity, the setting for these heaters will deviate from the configuration used during ground tests. The needed temperature setpoint and homogeneity to perform a measurement had been set to:

$$|T_l - T_w| \leq 0.5\,\mathrm{K} \tag{5}$$

$$\max(|T_l - T_i|) \leq 0.5\,\mathrm{K} \tag{6}$$

$$|T_l - T_{set}| \leq 0.1\,\mathrm{K} \tag{7}$$

where T_l is the liquid temperature, T_w is the wall temperature, T_i are the temperatures measured by the various temperature sensors inside the liquid, and T_{set} is the desired temperature. In this case the wall temperature T_w describes the temperature of the sensors inside the aluminum housing, and not the temperature of the substrate heater measured by the infrared camera. The liquid temperature, T_l, is calculated as the average value of at least 4 temperature sensors inside the liquid of which one near the inlet, one near the outlet, and two in the stagnant zone. Similarly, the wall temperature, T_w, is calculated as the average of temperature sensors inside the cell housing. Once the

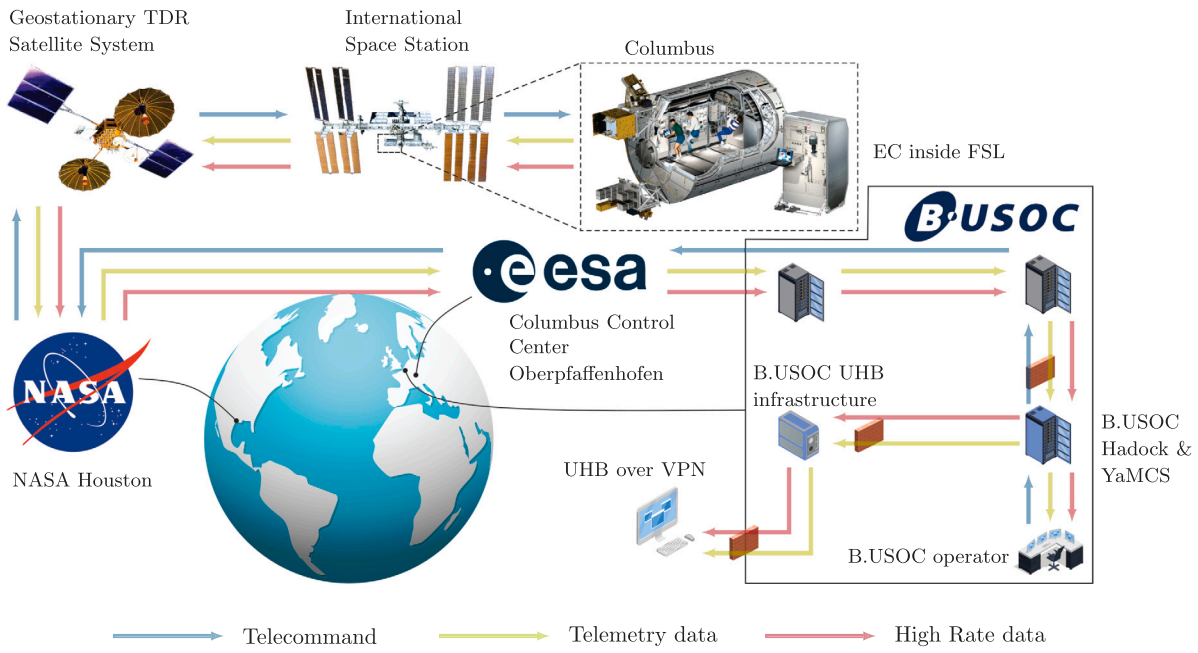

Fig. 7. High level overview of the end-to-end data flow, showing the Telemetry and Telecommand flow and High Rate Data path.

liquid has the desired temperature within the allowed levels of accuracy and homogeneity, the pressure is lowered to the experiment pressure and the substrate heater activated at the desired heat flux level. The laser pulse was activated at 1 s, 2 s, 3 s, 5 s, 10 s, 15 s, 20 s, and 25 s, after the activation of the substrate heater. This was repeated for 3 different values of laser pulse duration, namely 5 ms, 10 ms, and 20 ms. From the results of these tests the science team could narrow down the parameter space of interest and define the final parameters for the science runs.

Science runs. For the first phase of the mission a total number of 674 experiments have been defined, of which 268 pool boiling, 103 shear flow, 255 electric field, and 48 shear flow and electric field. Each experiment has been repeated at least three times. This resulted in a total of more than 2000 runs. During one science run, 5000 black and white images are recorded at 500 frames per second. The recording starts 1s before the laser pulse. In parallel 2400 infrared images are recorded at 240 fps. Temperature data from the MTCR sensors are available at 2000 Hz from the activation of the substrate heater until the end of the experiment, which is typically 9 s after the laser pulse. In total, one science run generates around 6.5 GB of data. This data is stored on the Video Monitoring Unit of the FSL rack and downlinked to ground using the High Rate Data Link at a maximum bandwidth of 32 Mbps. On the black and white images a PNG lossless level 3 compression is applied, reducing the data to 2.5 GB per run. The science data as well as the real-time telemetry (1 Hz housekeeping and health, and status data) are stored on the servers at B.USOC and are available to the science team. During the on-orbit execution some technical problems arised. For most of them a work around could be found not jeopardizing the mission objectives. However, two failures had significant impact on the scientific scope of the experiment: the failure of the high-speed IR camera and the blocking of the MTCR movement. The issue with the MTCR occurred right after the completion of the commissioning, and it was no longer possible to lower the MTCR to the desired position above the substrate heater. The MTCR was then left in the homing position for the rest of the campaign. The infrared camera was lost when 59% of the first mission was completed, with science data already available for all the 4 types of experiments. Within the second mission more than 1000 runs were performed similarly to the first mission with slightly adapted parameters, following the evaluation of the data from the first mission by the science teams. For appr. 50 experiments, the frame rate of the camera was halved in order to double the recording duration. For investigations using an electric field, an additional option was created to switch the electric field on or off during the experiment.

The 10-dimensional parameter space mentioned above can be reduced to 7 parameters for scientific analysis. Pressure and saturation temperature are separated from each other for operational reasons but can be converted into each other for scientific analysis. The height of the MTCR is omitted due to the defect mentioned in Section 3.3 in the early phase of the first campaign. The laser's pulse duration was set to 20 ms after completion of the fine-tuning, with a few exceptions, and is therefore not a variable in the scientific evaluation. The parameters used in both phases in the four main areas of investigation (pool boiling, shear flow, electric field, shear flow + electric field) are summarized in Fig. 8. The different parameters can be seen on the x-axis. The numbers in the individual boxes indicate the corresponding value of the parameter. On the y-axis, the number of runs performed with this value is plotted in stacked form. The coloring of a box shows the percentage distribution of this number among the 4 main areas of investigation.

3.4. Data evaluation

Most of the measured data is provided to the scientists in calibrated form and readable format. Otherwise, the conversion tools required for this purpose are given, or a detailed description is presented to convert the raw data. These include thermocouple and Pt100 temperature measurements, pressure sensor data, gravity data, synchronization data, facility and process parameters, just to name a few. All these data can be obtained by the data streams shown in Fig. 7. For further scientific evaluation, especially the data of the black and white camera as well as the available data of the infrared camera must be subjected to additional post-processing and analysis. These are summarized in the following two sections. Regarding the black and white data, the size and shape of the bubble are in the foreground; regarding the infrared data, the subsequential calculation of the heat flow is of interest.

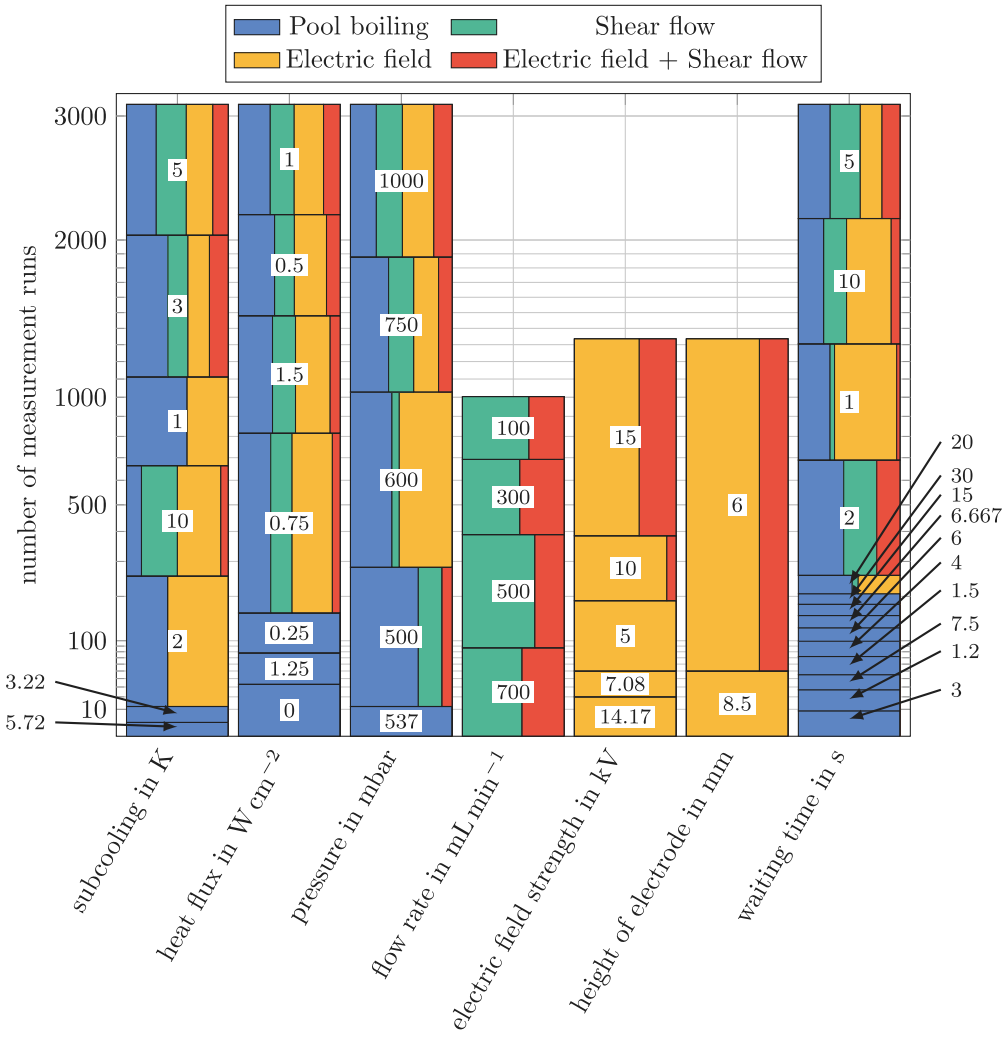

Fig. 8. Distribution of scientific parameters with respect to the four main areas of investigation (pool boiling, shear flow, electric field, shear flow + electric field). Each column is sorted by the amount of measurement taken at the specific parameter (number inside the box).

3.4.1. Black and white images

Images obtained from multiscale boiling experiment include several properties that make the accurate detection of bubbles' contour a challenging image analysis problem. These are:

- Light from the light source can reflect on the bubbles' interface causing specular highlights at the bubbles contour. This can cause a very low contrast at the actual location of bubbles' contour, while reinforcing high gradient at spurious locations.
- Self-reflections of the bubbles and the substrate on the bubbles' surface.
- The superheated fluid layer (especially close to the heated substrate) causes a gradient in the optical refraction index of the fluid. Hence the bubbles' shape can be distorted due to this non-uniform temperature profile of the surrounding liquid.

The steps of applied image processing algorithm are briefly described hereafter. The input to the computation is named image I (Fig. 10(a)). A coarse silhouette (blob) approximation of the bubble is obtained through background subtraction of the current image with the initial frame of the scene (Fig. 10(b)). A curve, C, is fitted to the points of its silhouette contour using least-squares method (Fig. 10(c)). Curve C is either a circle or an ellipse depending on user input and is not related to the real shape of the bubble but rather to its appearance in the image. Due to optical distortion, a spherical bubble that would appear ideally as a circle, may be better approximated in the image by an ellipse. As further clarified below, this choice regards solely the image approximation of the bubble and not the 3D interpretation of this measurement. A coarse-to-fine approach follows to detect the baseline of the bubble, using its reflection. The image row where the baseline occurs is initially localized at the bottom of the silhouette contour. A local optimization refines this localization, measuring vertically the symmetry in image intensities above and below the candidate image row b_c. The sum of absolute differences across the corresponding pixels as defined from the reflection of each candidate row, is used as the cost function. Contact points estimates, p and q, are initially guided by the intersections of C with row b_c. The Harris operator [32] is computed in their neighborhoods and the strongest local maximum in each of them is found. The final baseline row, b, is the average of the y-coordinates of these maxima (Fig. 10(d)).

The contour of the bubble is then detected. The region surrounding curve C is warped in a rectangular polar image V, where columns correspond to the circumference of C. According to the chosen C shape, circle or ellipse, this region is respectively an annulus or an elliptical ring.

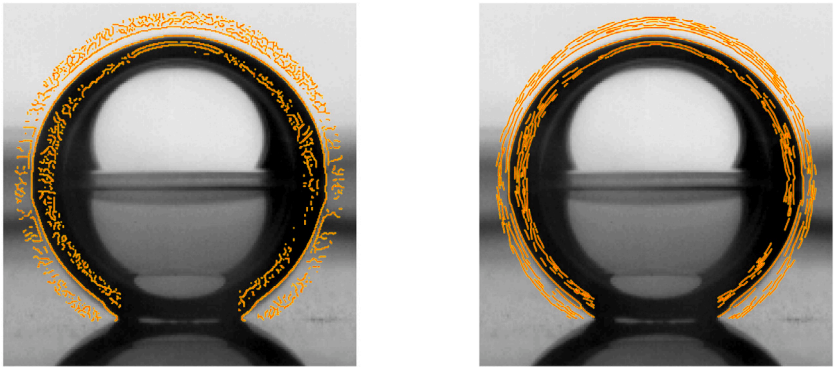

Fig. 9. Comparison of the detected edges (orange lines) for the conventional Canny method (left) with the proposed advanced method for bubble shapes (right). The edge detection is just performed close to the bubble's interface (see Fig. 10(c)).

Edge detection in image V is simplified as follows. The magnitude of V vertical gradient is computed and its local extrema are detected across the columns with sub-pixel accuracy. The resultant locations are treated as image edges. In order to detect even the faintest edges that may be part of the contour, the detection of local extrema is set to be sensitive even to minute amplitude. However, this effect is reduced since only the vertical direction in V corresponds to the radial direction, with respect to C, in I. The result of the proposed edge detection method is compared against the widest-used generic edge detection method [33], using the same extremum detection sensitivity, as shown in Fig. 9. In that figure, the detected edges using the conventional and the proposed method are superimposed as colored dots. Connected edges are then linked into segments based on 8-neighbor connectivity and disallowing connectivity in cases of junctions (edges with more than one neighbor) (Fig. 10(e)). The obtained segments are evaluated as to their compatibility to the shape of the bubble. This compatibility is determined by their curvature profile, as segments with bents do not comply to the smooth bubble contour and convexity. In addition, outlier segments with large distances from the size-dominant segments are also removed. Finally, the outmost of the segment points, if any, per each polar direction is the boundary point detection for that bearing. The result is a clockwise-ordered set of points forming a contour (Fig. 10(f)). Given the points of the boundary detection, several choices for approximating bubble contour with a curve are available (Fig. 10(g)). This curve is independent of C used to detect contour points and its selection is driven by the operator. The following approximations are currently employed: (a) One circle, based on the full contour, (b) One circle, based on the top-half contour, (c) Two circles, based on the left-half and right-half of the contour, and (d) One ellipse, based on the full contour. The different approaches can be chosen accordingly for the pool boiling, shear flow, and electric field cases due to the different bubble shapes to achieve an optimized result. An overview of the aforementioned computational steps is shown in Fig. 10. The figure shows the original image (a) on the top. The six images below illustrate the algorithmic steps, zooming in the image region where the bubble appears. The first image (b) shows the coarse silhouette obtained through background subtraction. In the second (c), curve C is superimposed in green color and the boundaries of the surrounding in blue and red. In the third step (d), the baseline row b and contact points p and q are plotted superimposed. Further, the third image shows the detected edges, and the fourth image (e) the segments of linked edges. The fifth image (f) shows the outermost of the segment points, and the sixth image (g) the fitted curve. In the last stage, a circle approximation is employed.

3.4.2. Infrared images

The significant benefit of the IR data is not only the pure measurement of the heater surface temperature, but even more the subsequent calculation of the heat flux from the heater to the fluid. Since the heat flux from the heater to the fluid depends on several factors, a more complex evaluation is required. The general procedure of this evaluation will be described in the following. A more detailed description of all individual points and an error analysis will be presented in future publications. There are so-called reference images for all measurements, which are taken before the heater is switched on. In most cases, the recording of the IR camera starts shortly before the nucleation is generated by the laser to distribute the available recording time as best as possible to the bubble growth. The heating phase, which can last several seconds, is therefore not measured. In some cases, especially in shear flow, the entire period from the heater on would be recorded by the IR camera. For these cases, the steps four and five of the following list can be neglected. The general approach for the calculation is as follows:

1. The raw infrared data are calibrated and filtered.
2. The temperature of the heater outside the field of view of the infrared camera during the runtime of the camera is calculated by averaging the measured temperature values over each streamwise position for every time.
3. The electrical power dissipation over the heater surface is calculated by using a finite element analysis to accurately capture the heat flux transferred to the liquid from the heater at every position.
4. The flow velocity profile in the liquid is calculated by numerical simulation based on the given parameter set.
5. The initial temperature of the heater is calculated. This is done by using the known preheat time (the time the heater was running, before the infrared data is collected), the volume flow rate in the liquid phase through the test cell, the flow profile, the (locally resolved) electrical heater output power, and the initial subcooling of the liquid in a finite element calculation. With these information, the heat transport in the heater and the heat transfer to the surrounding liquid phase is assessed and the resolved temperature of the heater for every preheat time is obtained. This step is decisive because the three-dimensional temperature distribution in the heater has a significant influence on the heat flow calculation. However, this cannot be measured and must therefore be calculated.
6. The heat flux is calculated with a finite element analysis of the entire heater. The previously obtained initial heater temperature is used as the initial condition, and the infrared data is used as

(a) Original image

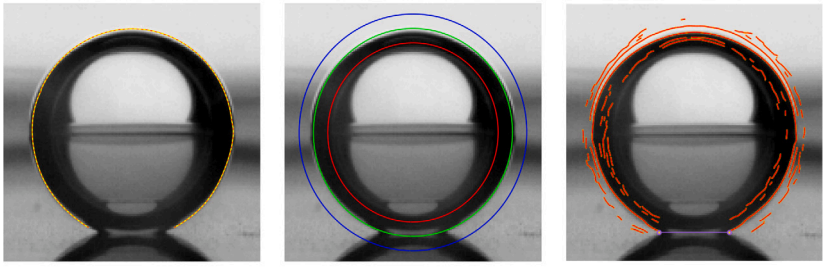

(b) Silhouette of the bubble by background subtraction

(c) Curve C (green) and boundaries of the bubble (red and blue)

(d) Previous picture with superimposed baseline row (b), contact point (p and q), and dectected edges

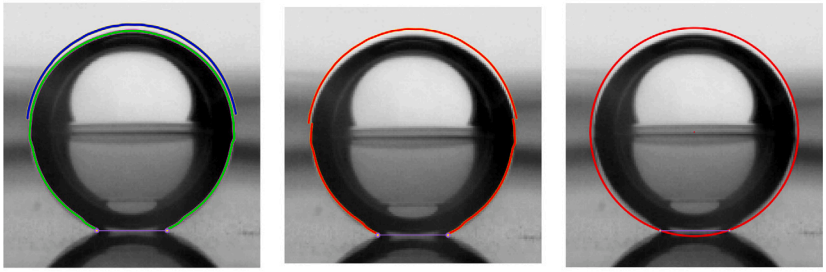

(e) Segment of the linked edges

(f) Outermost of the segment points

(g) Fitted curve by circle approximation in this case

Fig. 10. Computational steps of black and white image processing pipeline.

a time dependent temperature boundary condition. By solving the transient heat conduction in the heater, the heat flux from the heater to the liquid is found. This heat flux is then corrected for the electrical heater input (see step number 3) and the heat input from the laser (from a dedicated measurement). To reduce the time required for computing, both parts are not included in the finite element analysis of this step.

Fig. 11 shows a picture of the black and white camera (top) with the corresponding calibrated temperature field (middle) and the calculated distribution of the heat flux density. The example is taken from a shear flow test series.

4. Initial results

The following section provides an insight into the results of the four study groups and presents a basic comparison of the individual forces on the boiling process. In Fig. 12 the influence of the different applied forces are shown for the same set of parameters (if applicable). For pool boiling (top left), the round, undisturbed shape of the bubble is clearly visible. The bubble does not move away from the substrate heater under the given conditions. Its growth is only affected by reaching an outer wall or by stopping the experiment. For the electric field (top right), the deformation of the bubble is clearly visible. It shows an elongated geometry. In addition, the electric field causes the bubble to depart from the substrate heater. Under the given conditions, the bubble departs after about 4.8 s. The influence of the shear flow is shown at the bottom left. It can be seen that the bubbles are carried along by the shear flow and leave the heater surface. Under the given conditions, about 3 bubbles per second depart from the nucleation site. The additional switching on of an electric field (bottom right) shows a secondary influence on the bubble formation under the given conditions. Similarly to the shear flow case, about 3 bubbles per second depart from the nucleation site. The size of the bubble is also similar. Later on, the bubbles are clearly accelerated by the electric field, which can be seen by the larger distances between the bubbles and also by the peculiar shape of the bubble at the highest distance from the nucleation site. The video for the corresponding illustration is available at https://doi.org/10.48328/tudatalib-618. In the following, the influences of the individual main branches will be discussed in more detail.

4.1. Pool boiling

For pool boiling without external forces such as shear flow or electric field, the bubbles can theoretically grow indefinitely in weightlessness. In the current experiment, they are primarily limited by the experimental execution duration and the cell's spatial limitation. Additionally, the minimal residual gravity or other instabilities may

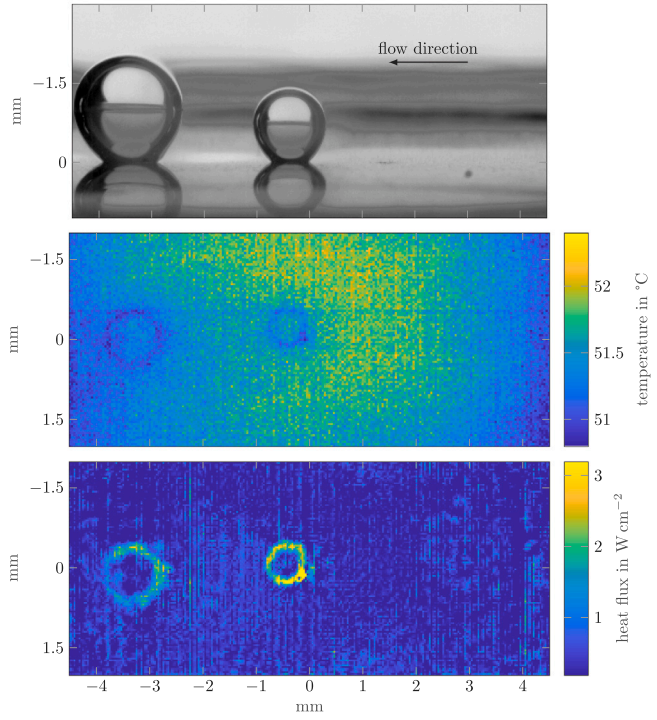

Fig. 11. Example calculation of the heat flux density distribution (bottom) based on the calibrated temperature field (middle) for a shear flow run. The top picture shows the corresponding BW image.

Table 2
Experimental parameters used in the reference runs.

p_l =	600 mbar
T_{sat} =	42.4 °C
T_{sub} =	3 °C
T_l =	39.4 °C
$qdot$ =	0.75 W cm^{-2}
t_{wait} =	5 s

cause the bubble to move slightly on the heater. Should the bubble leave the artificial nucleation site by this movement, new bubbles will form at this site, and bubble coalescence will occur. This can lead to further motion as well as oscillations of the bubble contour.

To check the experiments' reproducibility over the long period, the so-called reference case was performed regularly during both campaigns. Overall 25 reference case runs had been performed on 9 different days. The parameters of the reference case are shown in Table 2. The reference case is carried out independently of the MTCR and the electrode's position not to frequently move the actuators. To the extent that this can affect the space available for bubble growth, only the early bubble growth times will be compared. Fig. 13 shows the bubble diameter versus time for 8 different reference case runs covering the whole period of the mentioned two campaigns. It can be seen that the bubble growth behaves very comparably for all the experiments performed. The reference case runs performed at the end of the second campaign show a slightly larger bubble volume. For all evaluated references case runs so far the deviation between all (including not shown) runs is 3.3%. It is calculated by averaging the quotient of standard deviation and mean bubble size at each time step.

Based on the described reference case, the influences of the main parameters (pressure, heat flux, waiting time, and subcooling) are shown in Fig. 14. The dashed green line represents the reference case. It can be seen that the heating power and the subcooling have the most significant influence on the bubble growth. Concerning the waiting time, it can be seen that a qualitatively different curve results for a very short waiting time. This can be explained as follows. The bubble is generated by the additional laser energy during ignition (177 mW for 20 ms). Subsequently, however, due to the short preheating time (1 s with 0.75 W cm^{-2}) and the existing subcooling (3 K), there is not yet enough energy available for the bubble to grow in a qualitatively comparable way to the other experiments. A smaller influence of the waiting time on the bubble growth can be seen for longer waiting times. The pressure has a less significant influence on the growth of the bubble in the used parameter range. This is because the energy provided for evaporation is comparable between the different cases. Different bubble sizes can be primarily attributed to a change in vapor density.

In summary, it can be said that the effects of the individual parameters correspond to expectations. The bubble size increases with increasing heating power, increasing waiting time, decreasing subcooling and decreasing pressure.

4.2. Shear flow

Unlike pool boiling, multiple consecutive bubbles were formed on the substrate heater during boiling in shear flow. The bubbles depart from the nucleation site by sliding along the heated wall. For high values of the heat flux, the frequency of bubble formation increases and the bubbles may coalesce. A summary of the shear flow runs with the coalescence events is presented in Fig. 18 and will be discussed below.

The temporal evolution of the bubble equivalent diameter at p_l = 750 mbar, T_{sub} = 5 K, $\dot{q}$= 1 W cm^{-2}, Q = 300 mL min^{-1}, and t_{wait} = 5 s is shown in Fig. 15. The corresponding image of the bubbles, for t = 4.4 s, is shown in Fig. 12. Once the laser pulse activated the nucleation site, this leads to the nucleation of a first bubble. When the bubble grows to a particular size, it detaches from its position and continues to slide on the substrate heater due to the shear flow. Sliding of the bubble away from its position allows the formation of a new bubble at the nucleation site, and the cycle continues. The vertical dashed lines in Fig. 15 correspond to the departure of the bubble from the nucleation site, by sliding along the wall. The detachment diameter of the bubbles increases with time, because the thickness of the thermal boundary layer is also increasing with time.

The variation of different geometrical parameters of the bubble (corresponding to the second nucleating bubble shown in Fig. 15) with time during the life-time of growth and sliding at p_l = 750 mbar, T_{sub} = 5 K, $\dot{q}$ = 1 W cm^{-2}, Q = 300 mL min^{-1} is shown in Fig. 16(a). Similar to the bubble equivalent diameter d_b, bubble foot diameter d_{bf} is also observed to increase with time, which is in contrast to the quasistatic growth of an injected air bubble with a contact line pinned at the injection hole as reported in the literature [34]. This can be attributed to the evaporation at the bubble foot during boiling. cg_x and cg_y are the coordinates of the center of gravity with respect to the nucleation site (O, inset image, Fig. 16(a)). cg_y follows a trend similar to the bubble diameter d_b, however, cg_x initially remains quasi-static followed by a gradual increase with time, indicating the detachment/sliding of the bubble away from the nucleation site with a constant velocity. It should be noted that the bubble continues to grow during the sliding motion as the substrate heater was maintained at the superheated condition due to continuous heating. The corresponding variations of the contact angles at the advancing and receding fronts are presented in Fig. 16(b).

The temporal evolution of the bubble growth shown in Fig. 15 follows the relation $d_b = c_{gr} t^{0.5}$, which is the characteristic of the heat-diffusion controlled bubble growth [35]. The constant c_{gr} captures the rate of bubble growth and depends on the temperature of the liquid and substrate heater, liquid properties and flow conditions [7,36,37]. Larger value of c_{gr} suggests relatively larger bubble growth rate. The plot of constant c_{gr} versus liquid flow rate Q at heat fluxes of $\dot{q}$= 0.5 W cm^{-2} and 1 W cm^{-2}, and at p_l = 750 mbar, T_{sub} = 5 K is shown in Fig. 17(a). Each data point corresponds to the average value of

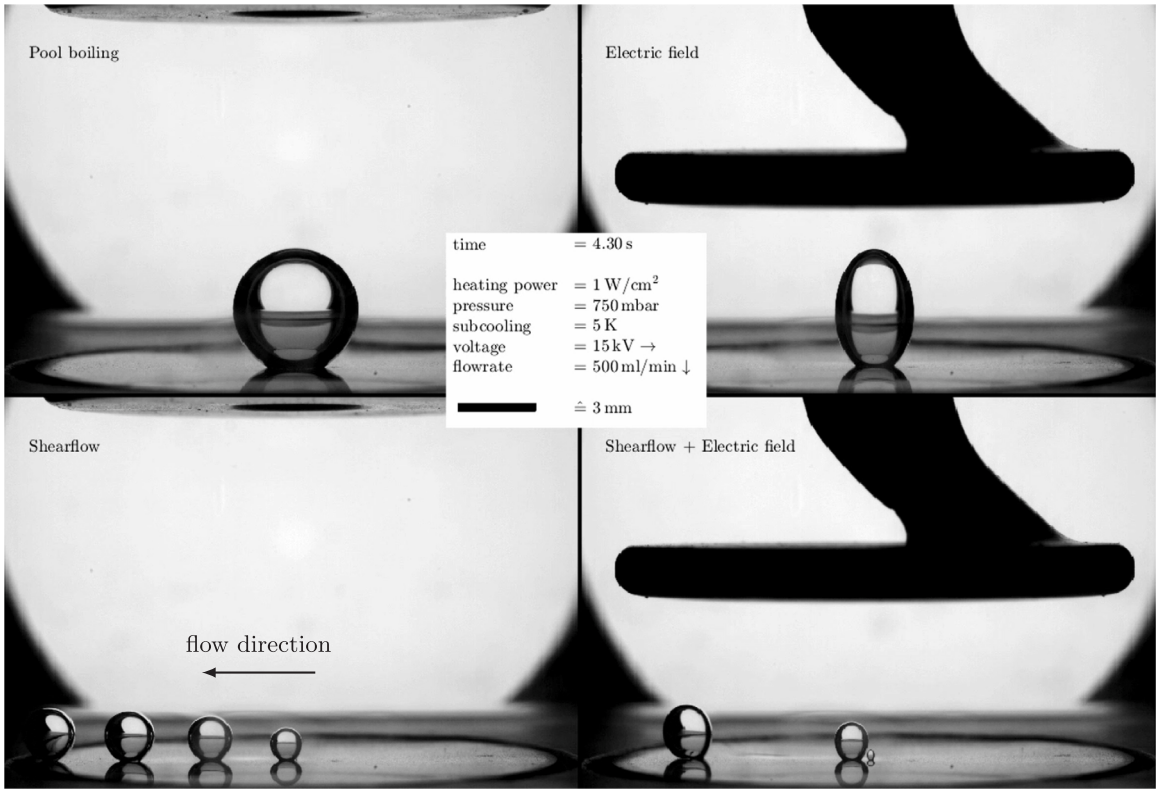

Fig. 12. Comparison of the different external forcing factors.

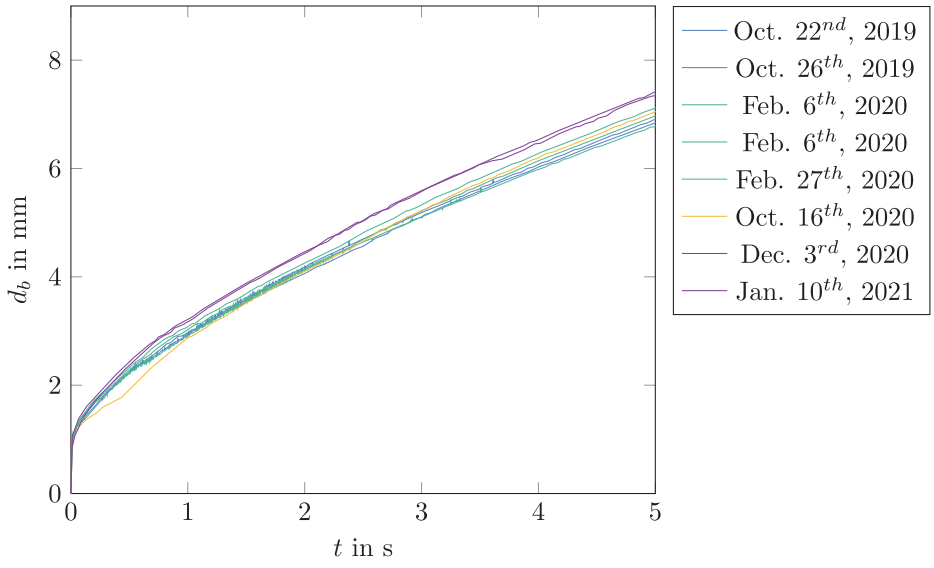

Fig. 13. Comparison of bubble diameter (resulting from circle fit approximation) for the pool boiling reference runs on different days during the mission.

c_{gr} for all the bubbles for a given experimental run (for instance, see Fig. 15) and error bar indicates the corresponding standard deviation. Heat transfer during subcooled boiling in microgravity condition is primarily governed by the evaporation in the contact line region and condensation at the bubble top [16]. Increase in the liquid flow rate results in the formation of a thinner superheated layer above the wall, which essentially reduces the evaporation at the contact line and in the near wall region. Moreover, the condensation of the bubble also increases due to increase in liquid flow rate and the exposure to relatively larger portion of the bubble to the subcooled liquid. The cumulative effect is to reduce the bubble growth rate. As a result, the value of c_{gr} gradually decreases with the increase in the liquid flow rate (Fig. 17(a),

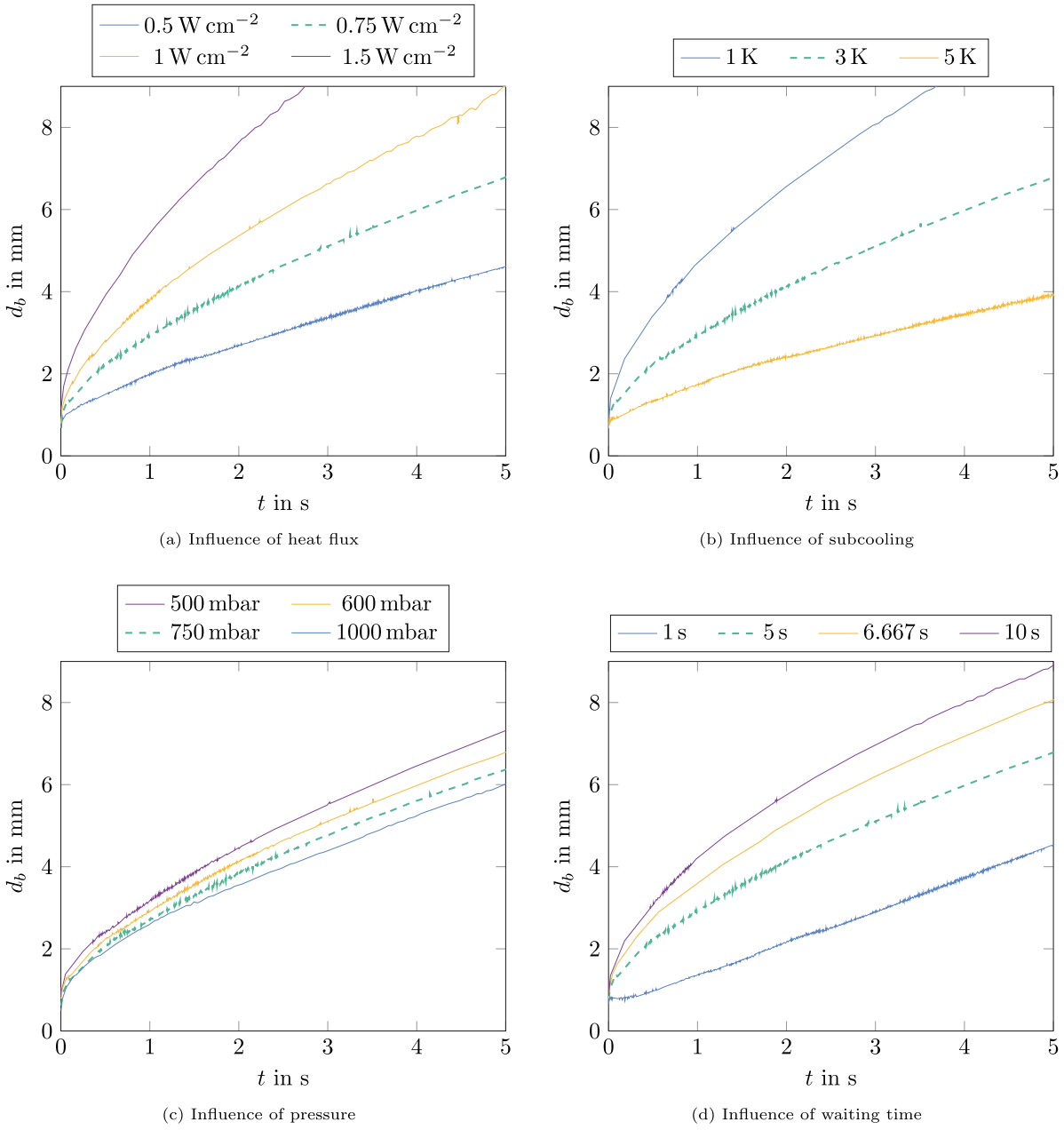

(a) Influence of heat flux

(b) Influence of subcooling

(c) Influence of pressure

(d) Influence of waiting time

Fig. 14. Comparison of the major influencing parameters on bubble growth based on the reference case conditions (dashed green line). In each diagram, the other parameters are as the reference case ones (cf. Table 2).

1 W cm^{-2}). Similarly, thickness of the superheated layer above the wall also reduces at lower heat flux values, leading to the decrease in the contact line evaporation. Consequently, relatively smaller value of c_{gr} at low heat flux (Fig. 17(a), 0.5 W cm^{-2}) can be attributed to the decrease in bubble growth rate due to the reduced superheated layer thickness. Moreover, the value of c_{gr} is not significantly changed by the liquid flow rate at low heat flux of 0.5 W cm^{-2}. This can be attributed to the relatively small thickness of the superheated layer above the wall.

The plot of the equivalent bubble departure diameter $d_{dep,eq}$ measured at the initiation of sliding motion versus liquid flow rates at heat fluxes of $\dot{q}$= 0.5 W cm^{-2} and 1 W cm^{-2} is shown in Fig. 17(b). As the bubble does not have a circular shape under the effect of external forces, the equivalent bubble diameter $d_{b,eq}$ is used in the following. Increased drag force on the bubble at larger flow rate causes early departure. Consequently, departure diameter decreases with the increase in flow rate.

Boiling experiments with a shear flow also opened an opportunity to study bubble coalescence and the effects associated with this phenomenon. Microgravity eliminates the buoyancy-induced differences in rise velocity between bubbles of different sizes [38], making the coalescence process less complex. Colin et al. [39] already proposed a model to predict bubble size distribution in a tube during bubbly flow in microgravity and found that coalescence significantly affects the bubble size. Apart from that, coalescence may also promote bubble lift-off due to an additional upward force that appears during the merger, which influences boiling heat transfer [40]. In normal gravity conditions, there are many experimental evidences proving that horizontal bubble coalescence may result in enhanced heat transfer and

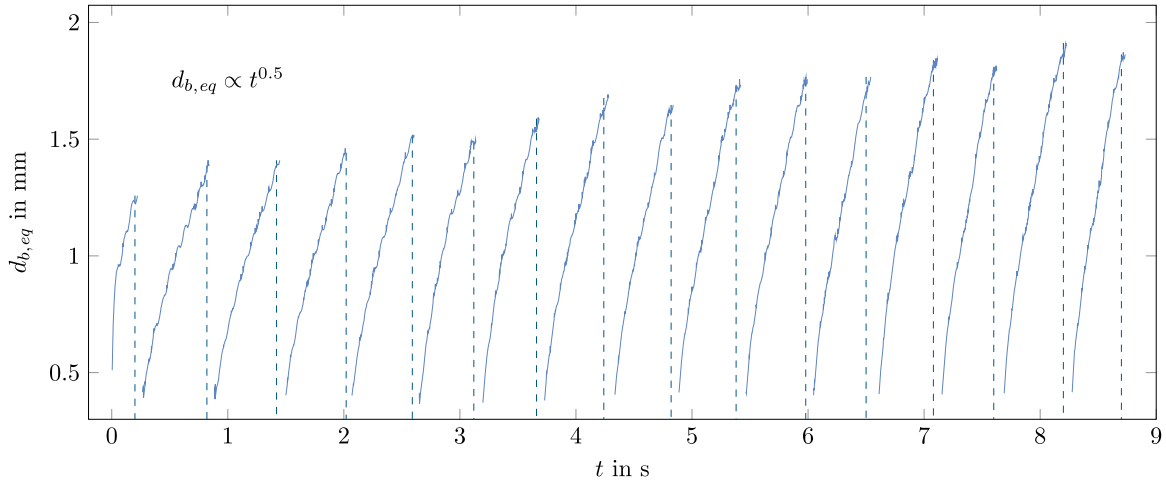

Fig. 15. The variation of bubble equivalent diameter with time. Vertical dashed line indicates sliding of bubble due to shear flow.

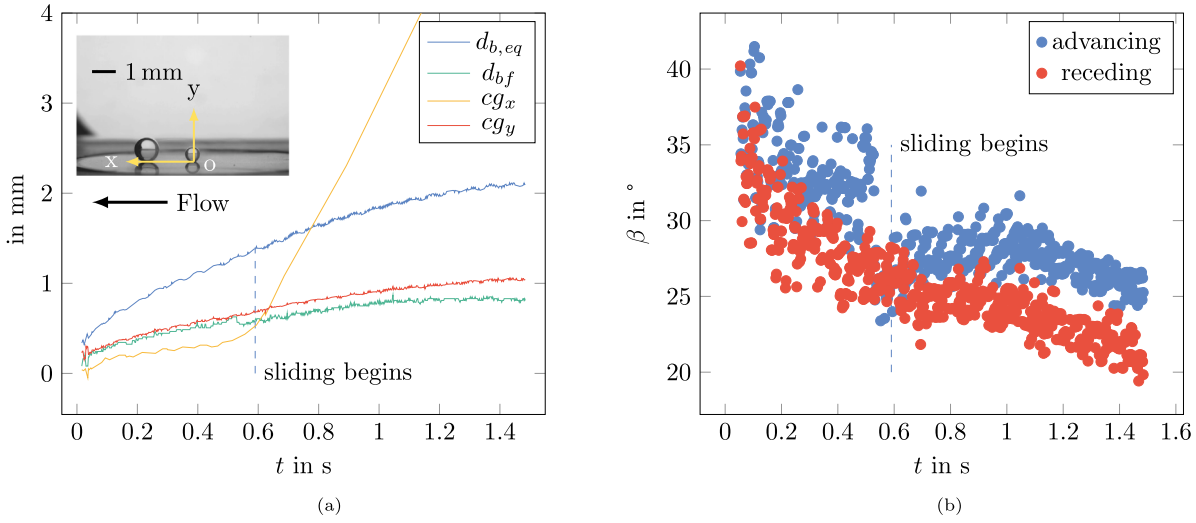

Fig. 16. The variation of bubble equivalent diameter, foot diameter, x and y-coordinate of center of gravity with time (a) and the corresponding contact angles (b).

faster liquid replenishment of active nucleation sites [41–44]. However, only few publications are available for microgravity conditions [45,46], none of them specifically focusing on coalescence in shear flow boiling. In-depth analysis of experimental result from both missions will provide new insights into the bubble coalescence phenomenon. Even though the designed boiling cell is not specifically targeting the bubble coalescence, the shear flow boiling provided a satisfactory number of bubble interactions. The Science team already identified experimental conditions under which the coalescence events are likely to occur. Out of the 84 analyzed experimental runs, 47 (i.e. 55.9%) of them exhibited one or more (up to 10) horizontal coalescence events, ranging from small two-bubble mergers to horizontal chain coalescence of several bubbles. The sunburst diagram in Fig. 18 shows from the center outward the effects of subcooling, heat flux, shear flow rate, waiting time and saturation temperature on detected bubble coalescence, respectively. First observations indicate that subcooling temperature together with heat flux are the dominating factors on the appearance of coalescence under shear flow conditions, followed by shear flow rate and waiting time. Initial results also show that saturation temperature (i.e. the system pressure) plays a minor role in the occurrence of coalescence event.

4.3. Electric field

During the first campaign the electric field was active during all phases of the experiment (heating of the surface for the duration of t_{wait}, laser pulse, bubble nucleation, growing and detachment). Within the second campaign the electric field was switched off during waiting time, laser pulse and bubble nucleation; then, at a defined time t_{on} it was switched on to be switched off after another amount of time t_{off}. Both experiment sequences are shown in Fig. 19. In the following it is referred to the first campaign, namely the electric field is kept always on. Fig. 20 shows the clear effect of different electric field levels on bubble shape, due to an additional electric stress applied at the liquid–vapor interface.

For some experiments (e.g. low subcoolings and high heat fluxes) at the lower values of electric field intensity the bubble grew too large and interacted with the electrode before detachment. It was decided to repeat those experiments moving the electrode at larger distance from the surface and keeping the same average intensity of electric field; furthermore, those runs give the opportunity to study the influence of the electrode geometrical configuration on the process.

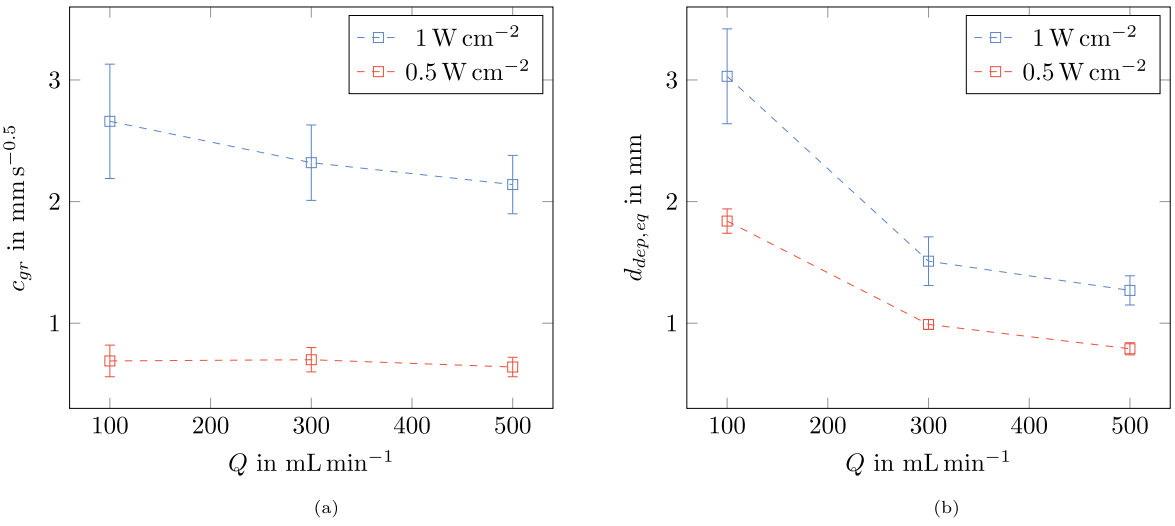

Fig. 17. (a) Constant c_{gr} and (b) bubble departure diameter versus liquid flow rate at heat fluxes of $\dot{q}$= 0.5 W cm^{-2} and 1 W cm^{-2}, and at p_l = 750 mbar, T_{sub} = 5 K.

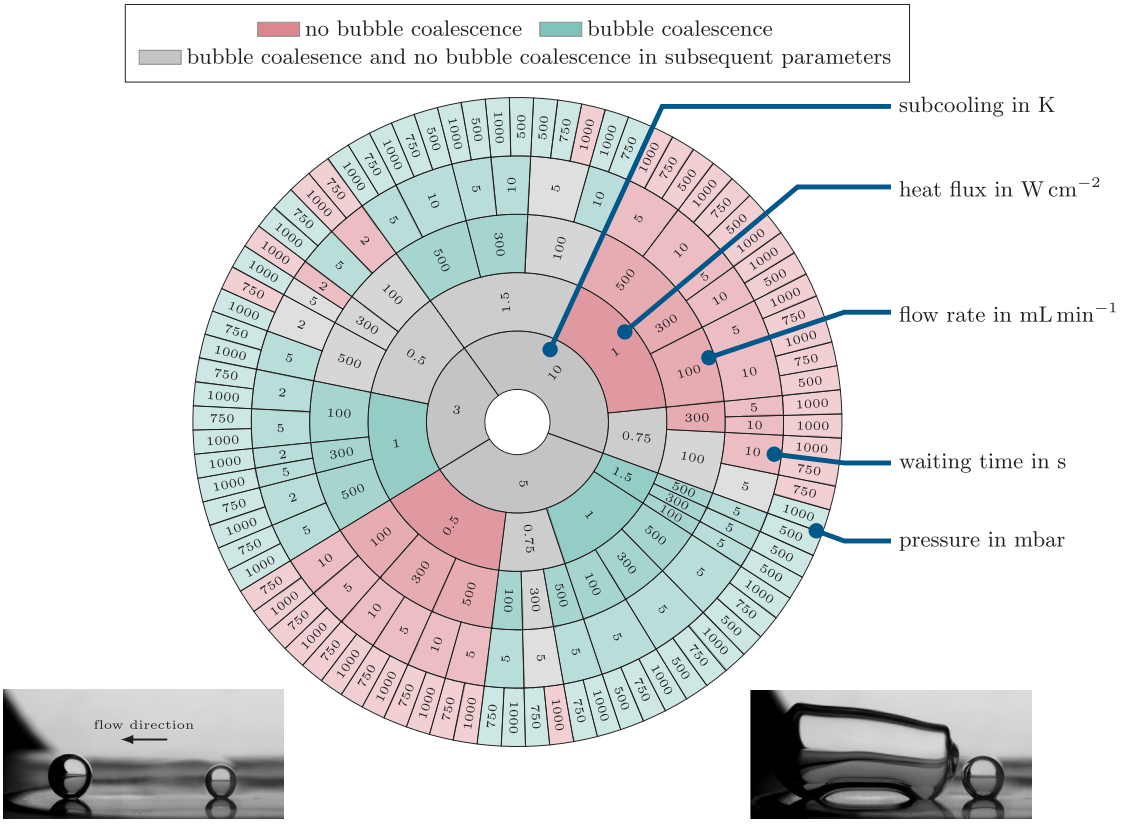

Fig. 18. The occurrence of shear flow bubble coalescence under various experimental conditions in microgravity. Experimental parameters of both pictures: left T_{sub} = 10 K, $\dot{q}$ = 1 W cm^{-2}, Q = 100 mL min^{-1}, t_{wait} = 10 s, p_l = 500 mbar - right T_{sub} = 5 K, $\dot{q}$ = 1 W cm^{-2}, Q = 100 mL min^{-1}, t_{wait} = 5 s, p_l = 500 mbar.

Fifty experiments were repeated with the electrode at 8.5 mm (instead of 6 mm) with applied voltages of 7.08 kV and 14.17 kV corresponding to a mean electric field intensity of 0.83 MV m^{-1} and 1.67 MV m^{-1}.

The images of the bubbles obtained through shadowgraphy using a BW camera were processed via a Matlab code. The bubble contour was detected and the most interesting geometrical parameters were recorded: bubble volume, bubble equivalent diameter, bubble foot diameter, bubble height, bubble curvature at the apex and bubble contact angle (example in Fig. 21). The bubble shape was influenced by the electric field at every time of the test: increasing the voltage, the bubble shape was increasingly elongated in vertical direction and compressed in radial direction (as already noted in [47,48]). With an applied voltage of 5 kV (corresponding to a field intensity of 0.83 MV m^{-1} for

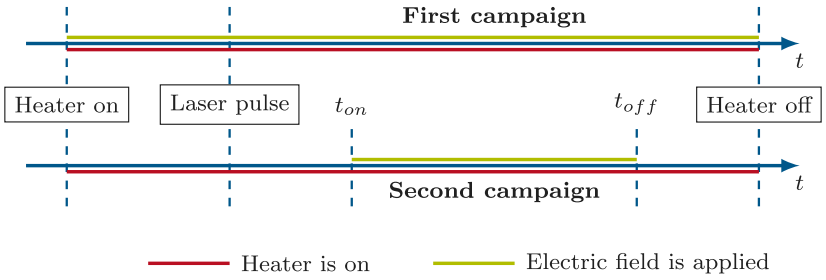

Fig. 19. Comparison of the electric field operation between the first and second campaign.

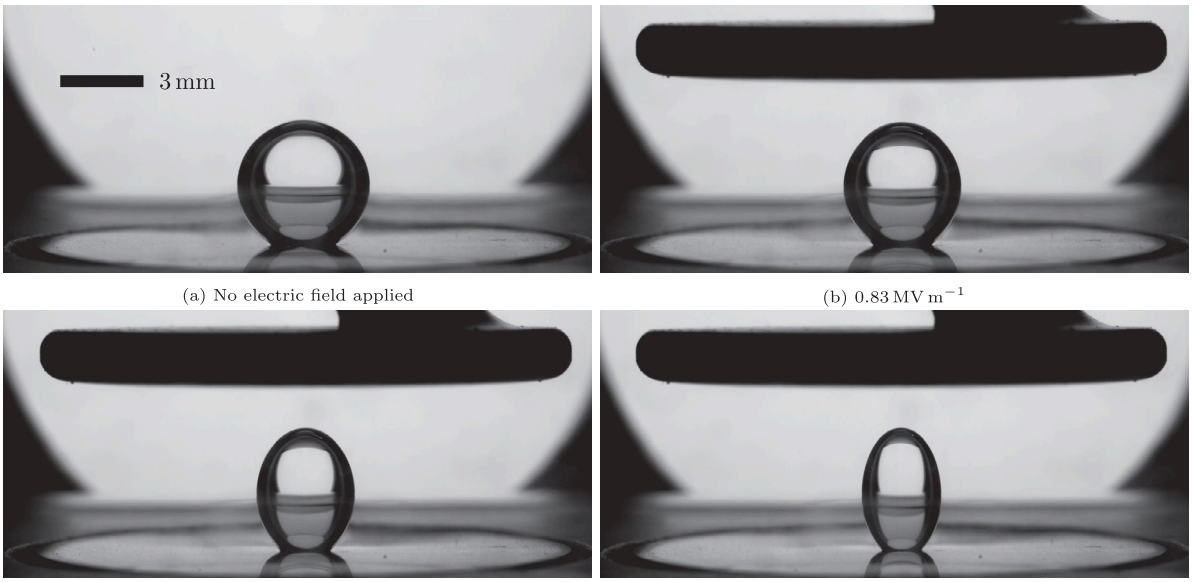

Fig. 20. Effect of the electric field on the bubble shape for different values of electric field intensity $E = U_{elec}/h_{elec}$.

a distance of 6 mm) the bubble shape was still nearly spherical. The most remarkable effect of the electric field is the bubble detachment (see Figs. 21 and 22), which always occurred when the bubble received enough energy to grow sufficiently in the amount of time available for the experiment (that was 9 s in total). Detachment occurred even for the lowest value of the electric field; detachment volume and detachment foot diameter decreased as the electric field increased and, consequently, the detachment frequency increased (see Fig. 22). The values of the detachment volume as a function of the electric field (for the same other input parameters) appeared to be constant and well reproducible, demonstrating the capability of electric field to promote regular bubble detachment in microgravity. After a small transitional period, also the detachment frequency became stationary. After detachment, the bubble was lifted off towards the electrode.

Using the geometrical parameters reported in Fig. 21, it is possible to calculate the forces acting on the bubble [47–49], namely force due to internal overpressure, force due to surface tension and inertial force, if not negligible. The unbalance of these known forces yields the experimental value of resulting force, to be compared later with numerical models of the electric force. An example of the experimental calculated forces is shown in Fig. 23.

4.4. Electric field + shear flow

The combined effect of shear flow and electric field was also investigated as an alternate strategy to remove bubble from the heater surface in the absence of buoyancy. Presence of electric field considerably influenced dynamics of bubble growth even in the presence of shear flow. The effect of electric field was to create a surface force, which elongates the bubble. Note that this elongation exposed the bubble to a higher velocity and may ease its detachment. Consequently, in contrast to the shear flow without electric field, bubbles were deformed in the presence of electric field to a nearly ellipsoidal shape with the major axis normal to the wall. The temporal evolution of the bubble height at $p_l = 750$ mbar, $T_{sub} = 5$ K, $\dot{q} = 1$ W cm^{-2} and intermediate flow rate of $Q = 300$ mL min^{-1} with and without electric field (voltage 15 kV) is shown in Fig. 24(a). When the size of the bubble was small, the effect of electric field was relatively less discernible whereas at larger size bubble deformation was more visible. This is evident from the relatively larger height (h) and larger h/d ratio in the presence of electric field, see Fig. 24(a) and 24(b), respectively.

Moreover, even in the presence of electric field bubbles continued to move along the direction of shear flow. No departure in the normal direction away from the wall was observed. However, at the low flow rate of $Q = 100$ mL min^{-1} relatively larger bubbles formed

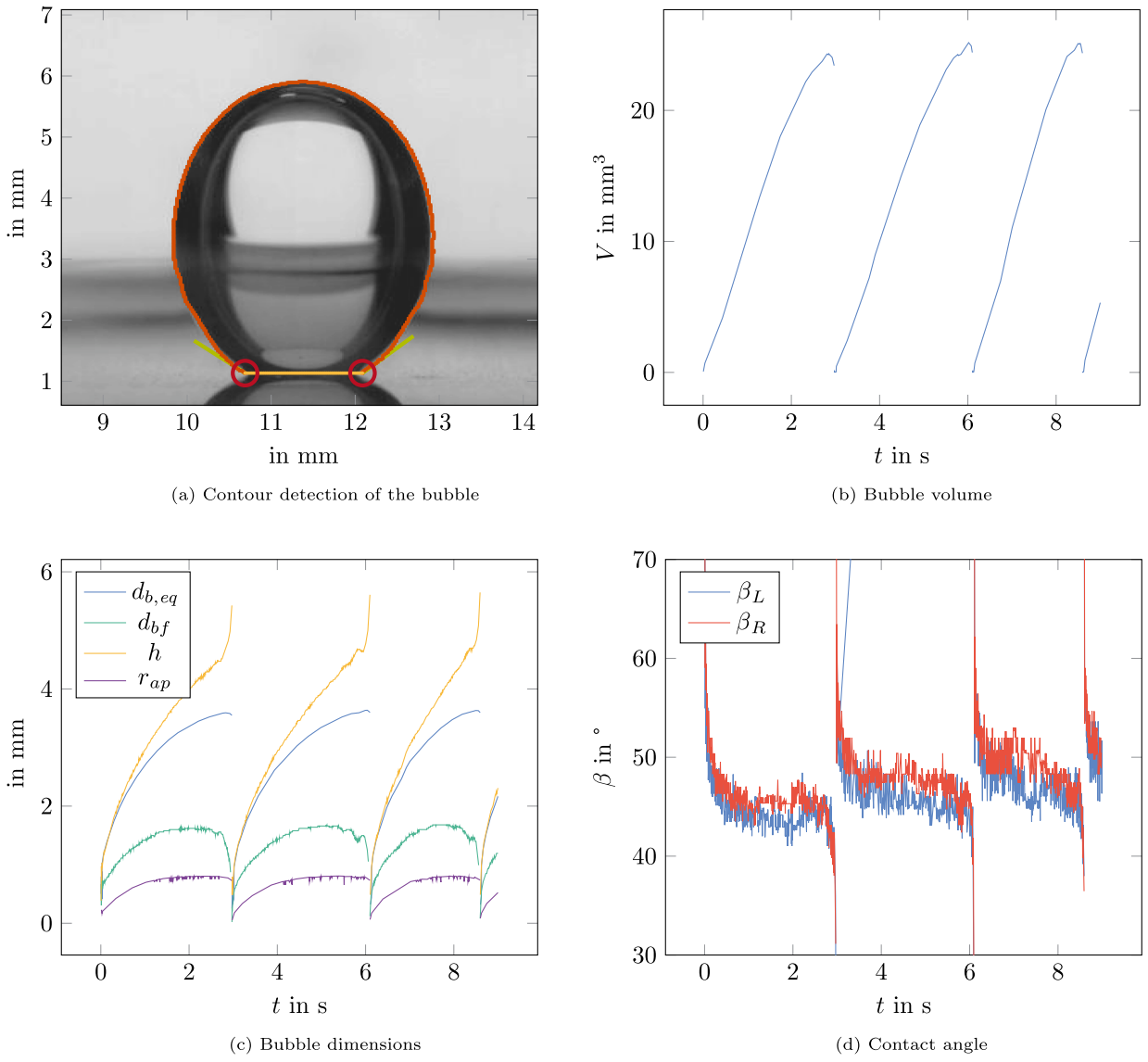

Fig. 21. An example of Matlab code edge detection process (a), bubbles volume (b), bubbles equivalent diameter, foot diameter, height and apex radius (c), left and right contact angles (d). Experimental parameters: $p_l = 600\,\text{mbar}, T_{sub} = 5\,\text{K}, \dot{q} = 0.75\,\text{W cm}^{-2}, t_{wait} = 10\,\text{s}, E = 2.5\,\text{MV m}^{-1}$.

in comparison with higher flow rate conditions, as the electric field force dominated over the drag force acting on the bubble due to the shear flow. This forced the bubble to depart in the normal direction away from the substrate without any sliding motion (see, Fig. 25), which was similar to the case of pool boiling with electric field. The video for the corresponding illustration is available at https://doi.org/10.48328/tudatalib-618. A more detailed analysis of these complex interrelationships will follow in future publications.

5. Conclusion

The Multiscale Boiling Project is the first experiment in the history of boiling research that combines both undisturbed bubble growth and the influence of external forces (namely shear flow and electric fields) within one facility. The project was conducted within two measurement campaigns on-board the International Space Station from 2019 to 2021. After completing the measurements, the experimental setup will be handed over to the Science Team for further investigations on ground in summer 2021. Despite the intermittent failures of the infrared camera and the blocked adjustment of the MTCR height, a majority of the objectives presented in Section 2.1 could be achieved. Objectives 1–4 were achieved within the conducted investigation. Bubble interactions (objective 6) were also observed and investigated. These were not initiated in a controlled way as such a feature was not included in the setup design for reasons of space. Rather they occurred in a more sporadic way in the studies related to objectives 1–4 and were captured by observations. The situation is similar with objective 5. The exchange or explicit addition of a second fluid were not possible under the imposed space restrictions. This objective is to be investigated with further ground tests and investigations, for example, in parabolic flights. In addition, the return of the EC enables the investigation of different gravity conditions with the otherwise same parameters as used on the ISS as well as a comparison to the experiments performed on ground during the SVT before the mission. Further experiments in long-term microgravity could give valuable insights into boiling mechanisms. Other liquid mixtures could be tested, coupled with IR camera measurement, allowing the validation of numerical models.

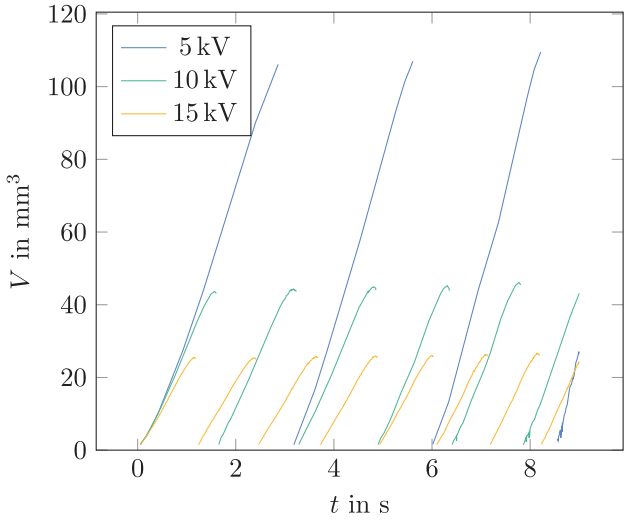

Fig. 22. Bubble volume and frequency for different strength of the electric field.

Within this publication, a first overview of the project as a whole was given. It explains the complex setup, the experiment execution on the ISS, and the significant aspects of the evaluation. In the context of initial analyzes, the high reproducibility of the experiments could be demonstrated in pool boiling by repeated execution of the reference case. Furthermore, the general trends observed regarding the variation of heat flux, waiting time, pressure, and subcooling correspond to the preliminary expectations. Among these parameters, the pressure level showed the weakest influence on bubble growth under otherwise comparable conditions. For experiments performed with a shear flow, a bubble grows at the cavity and departs by sliding along the heated surface. This process continues cyclically. The bubbles' size and frequency of formation depend on the heat flux, the liquid flow rate, and subcooling. When the frequency of detachment of the bubble is high enough, coalescence events between sliding bubbles are observed. The primary outcome of electric field runs is demonstrating its capability to promote stable bubble detachment even in microgravity. The detachment volume depends on electric field intensity, while detachment frequency is a function of other parameters, such as pressure, subcooling, and mainly heat flux and thermal boundary layer extension (waiting time). The effectiveness in continuously removing vapor from the heated surface was demonstrated successfully. The next steps will focus on a detailed analysis of bubble dynamics, force and stress balances, detachment mechanisms, and heat transfer rates to highlight and quantify the differences with bubble dynamics in terrestrial conditions. The combined effect of shear flow and the electric field was also investigated as an alternate strategy to remove bubbles from the heater surface in the absence of buoyancy. Under the electric field effect, the bubble is elongated perpendicularly to the substrate and thus exposed to a higher velocity of the shear flow, promoting its detachment. For the lowest flow rate, the bubble is detached perpendicularly to the substrate due to the dominant effect of the electric field. For moderate and high flow rates, the bubble is elongated but does not detach from the substrate. Instead, the bubble departs from the nucleation site by sliding along the substrate. In the following analyzes, the forces on the bubble are to be investigated in more detail, and, if possible, a boundary map is to be created under which conditions breakage from or slipping along the substrate occur.

In the future, it is planned to publish further detailed descriptions of the individual aspects like the design details, the heat transfer calculation, and the image processing of the black and white data, in addition to the scientific results themselves. Therefore, several groups of the Science Team are dealing with data processing and analysis and have already launched a benchmark study for image data post-processing of bubble growth characteristics in four directions. Namely: pool boiling, shear flow, electric field, and the combined effect of shear flow and electric field. In order to be able to evaluate the horrendous amount of data, further work is being done on sharing and optimizing evaluation algorithms and procedures. With the large amount of data available, each group of the Science Team will investigate the physics of bubble behavior in several operating conditions. Several joint papers will be published in the near future, focusing on specific aspects of the bubble behavior in various situations. Finally, all these results will be used for better understanding and modeling of the boiling processes.

Declaration of competing interest

Peter Stephan reports financial support was provided by German Aerospace Center. Catherine Colin reports financial support

Acknowledgment

The present work has been carried out in the framework of the European Space Agency Research Projects AO-2004-111: BOILING, AO-1999-110: EVAPORATION, AO-2004-096: CONDENSATION. We thank all the Multiscale Boiling Science Team Members of the different institutions involved:

Technical University of Darmstadt, Institute for Technical Thermodynamics
Aix-Marseille University, IUSTI
University of Pisa
Institute of Thermal-Fluid Dynamics, ENEA
Institut de Mécanique des Fluides de Toulouse, University of Toulouse
Aristotle University of Thessaloniki
Institute of Computer Science, FORTH
Transfers, Interfaces and Processes, Université libre de Bruxelles
University of Ljubljana
LAboratoire PLAsma et Conversion d'Energie
University of Padova
Kutateladze Institute of Thermophysics, Novosibirsk
University of Hyogo
Kyushu University
Kobe University

for their contribution in making possible the implementation of the experiment on-board the International Space Station, the authors would also like to gratefully thank ESA, and in particular Olivier Minster, Anne Pacros, Balázs Tóth, and Marco Braibanti for their interest and support to the activities linked to Multiscale Boiling, and for the fruitful discussions. The authors would also like to thank AIRBUS (with particular gratitude to the project manager, Olaf Schoele-Schulz), as well as B.USOC for the kind cooperation during all the pre-flight, in-flight and post-flight operations.

Co-authors from the Technical University of Darmstadt would like to thank the German Aerospace Center (DLR) for the financial support in the framework of the Vapor II project, grant no. 50WM1959. Co-authors from the Institut de Mécanique des Fluides de Toulouse would like to thank the French Space Agency CNES for its support through a post-doc grant, funding, and organization of parabolic flight campaigns. Co-authors from the University of Ljubljana would like to acknowledge funding by the Slovenian Research Agency (P2-0223 and J2-2486). Co-authors from the Kutateladze Institute of Thermophysics would like to acknowledge funding by the Russian Science Foundation (Project No. 19-19-00695). Co-authors from IUSTI would like to thank the French Space Agency CNES for its funding and support of boiling experiments. Co-authors from the Université libre de Bruxelles would like to acknowledge the financial support from BELSPO (PRODEX Heat Transfer).

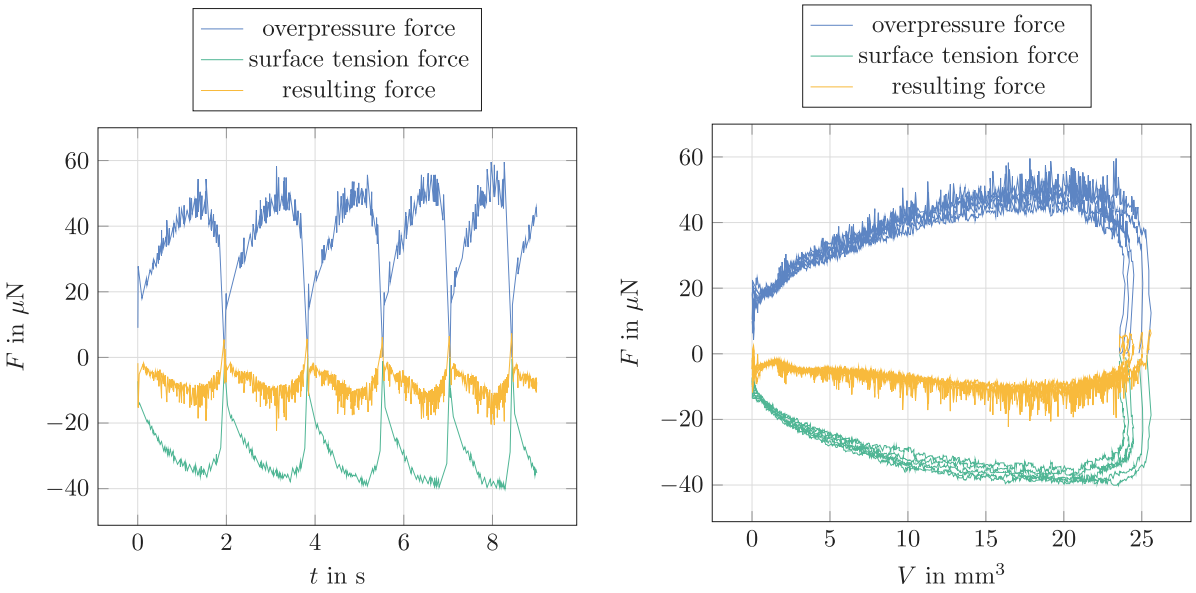

(a) Force on the bubble over time (b) Force on the bubble versus bubble volume

Fig. 23. Vertical force balance on bubbles. Experimental parameters : p_l = 1000 mbar, T_{sub} = 5 K, $\dot{q}$= 1 W cm^{-2}, t_{wait} of 10 s, E = = 2.5 MV m^{-1}.

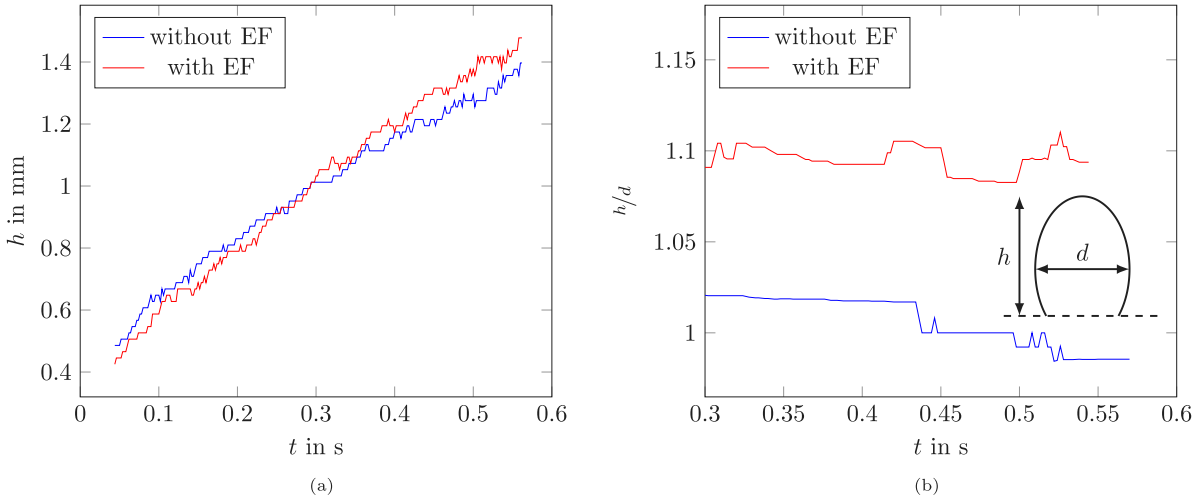

(a) (b)

Fig. 24. The plot of (a) bubble height and (b) h/d ratio versus time, where d is diameter measured parallel to the substrate (shown in (b)) during boiling with and without electric field.

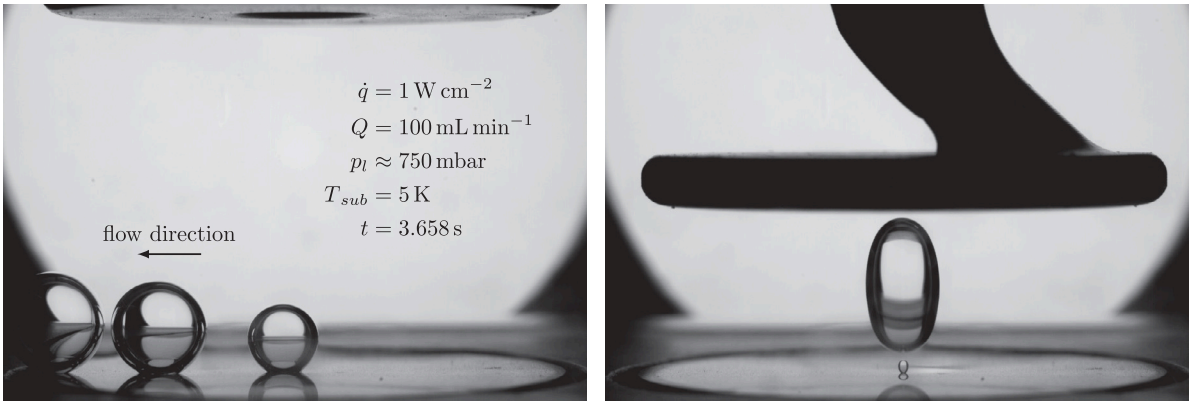

(a) Shear flow (b) Shear flow and electric field

Fig. 25. Comparison of bubble behavior during boiling with (a) shear flow and (b) shear flow with electric field at low flow rate of Q = 100 mL min^{-1}.

References

[1] S. Nukiyama, The maximum and minimum values of the heat q transmitted from metal to boiling water under atmospheric pressure, J. Soc. Mech. Eng. (206) (1934) 367–374.

[2] H.K. Forster, N. Zuber, Growth of a vapor bubble in a superheated liquid, J. Appl. Phys. 25 (4) (1954) 474–478, http://dx.doi.org/10.1063/1.1721664.

[3] K. Engelberg-Forster, R. Greif, Heat transfer to a boiling liquid—mechanism and correlations, J. Heat Transfer 81 (1) (1959) 43–52, http://dx.doi.org/10.1115/1.4008129.

[4] S.S. Kutateladze, Boiling heat transfer, Int. J. Heat Mass Transfer 4 (1961) 31–45, http://dx.doi.org/10.1016/0017-9310(61)90059-X.

[5] W.M. Rohsenow, A Method of Correlating Heat Transfer Data for Surface Boiling of Liquids, Technical Report, No. 5, Massachusetts Institute of Technology, Heat Transfer Laboratory, 1951, URL http://hdl.handle.net/1721.1/61431.

[6] C.-Y. Han, P. Griffith, The mechanism of heat transfer in nucleate pool boiling - Part I, Int. J. Heat Mass Transfer 8 (6) (1965) 887–904, http://dx.doi.org/10.1016/0017-9310(65)90073-6.

[7] M.G. Cooper, The microlayer and bubble growth in nucleate pool boiling, Int. J. Heat Mass Transfer 12 (8) (1969) 915–933, http://dx.doi.org/10.1016/0017-9310(69)90155-0.

[8] K. Stephan, M. Abdelsalam, Heat-transfer correlations for natural convection boiling, Int. J. Heat Mass Transfer 23 (1) (1980) 73–87, http://dx.doi.org/10.1016/0017-9310(80)90140-4.

[9] D. Gorenflo, D. Kenning, H2 pool boiling, in: VDI Heat Atlas, Springer Berlin Heidelberg, Berlin, Heidelberg, 2010, pp. 757–792, http://dx.doi.org/10.1007/978-3-540-77877-6_45.

[10] V.K. Dhir, Nucleate and transition boiling heat transfer under pool and external flow conditions, Int. J. Heat Fluid Flow 12 (4) (1991) 290–314, http://dx.doi.org/10.1016/0142-727X(91)90018-Q.

[11] P. Stephan, B1 fundamentals of heat transfer, in: VDI Heat Atlas, Springer Berlin Heidelberg, Berlin, Heidelberg, 2010, pp. 15–30, http://dx.doi.org/10.1007/978-3-540-77877-6_115.

[12] R. Raj, J. Kim, J. McQuillen, Gravity scaling parameter for pool boiling heat transfer, J. Heat Transfer 132 (9) (2010) 091502, http://dx.doi.org/10.1115/1.4001632.

[13] R. Siegel, Effects of reduced gravity on heat transfer, in: J.P. Hartnett, T.F. Irvine (Eds.), in: Advances in Heat Transfer, vol. 4, Elsevier, 1967, pp. 143–228, http://dx.doi.org/10.1016/S0065-2717(08)70274-0.

[14] T. Oka, Y. Abe, K. Tanaka, Y.H. Mori, A. Nagashima, Observational study of pool boiling under microgravity, JSME Int. J. II 35 (2) (1992) 280–286, http://dx.doi.org/10.1299/jsmeb1988.35.2_280.

[15] J. Straub, M. Zell, B. Vogel, Pool boiling in a reduced gravity field, in: Proceeding of International Heat Transfer Conference 9, Begellhouse, Connecticut, 1990, pp. 91–112, http://dx.doi.org/10.1615/IHTC9.1860.

[16] O. Kannengieser, C. Colin, W. Bergez, Influence of gravity on pool boiling on a flat plate: Results of parabolic flights and ground experiments, Exp. Therm Fluid Sci. 35 (5) (2011) 788–796, http://dx.doi.org/10.1016/j.expthermflusci.2010.04.010.

[17] N. Schweizer, P. Di Marco, P. Stephan, Investigation of wall temperature and heat flux distribution during nucleate boiling in the presence of an electric field and in variable gravity, Exp. Therm Fluid Sci. 44 (2013) 419–430, http://dx.doi.org/10.1016/j.expthermflusci.2012.08.002.

[18] S. Fischer, S. Herbert, A. Sielaff, E.M. Slomski, P. Stephan, M. Oechsner, Experimental investigation of nucleate boiling on a thermal capacitive heater under variable gravity conditions, Microgravity Sci. Technol. 24 (3) (2012) 139–146, http://dx.doi.org/10.1007/s12217-011-9273-6.

[19] H. Ohta, M. Kawaji, H. Azuma, K. Inoue, K. Kawasaki, S. Okada, S. Yoda, T. Nakamura, Heat transfer in nucleate pool boiling under microgravity condition, in: Heat Transfer Conference, vol. 2, 1998, pp. 401–406, URL http://www.dbpia.co.kr/journal/articleDetail?nodeId=NODE00337809.

[20] O. Kannengieser, C. Colin, W. Bergez, Pool boiling with non-condensable gas in microgravity: Results of a sounding rocket experiment, Microgravity Sci. Technol. 22 (3) (2010) 447–454, http://dx.doi.org/10.1007/s12217-010-9211-z.

[21] C. Colin, O. Kannengieser, W. Bergez, M. Lebon, J. Sebilleau, M. Sagan, S. Tanguy, Nucleate pool boiling in microgravity: Recent progress and future prospects, C. R. Mec. 345 (1) (2017) 21–34, http://dx.doi.org/10.1016/j.crme.2016.10.004.

[22] H. Lee, Herman Merte Jr., F. Chiaramonte, The pool boiling curve in microgravity, in: 34th Aerospace Sciences Meeting and Exhibit, American Institute of Aeronautics and Astronautics, Reston, Virigina, 2012, p. 01151996, http://dx.doi.org/10.2514/6.1996-499.

[23] S.M.M. Steinbichler, J. Straub, Nucleate boiling heat transfer on a small hemispherical heater and a wire under microgravity, in: Heat Transfer Conference, vol. 2, 1998, pp. 539–544, URL http://www.dbpia.co.kr/journal/articleDetail?nodeId=NODE00337832.

[24] J.-F. Zhao, J. Li, N. Yan, S.-F. Wang, Bubble behavior and heat transfer in quasi-steady pool boiling in microgravity, Microgravity Sci. Technol. 21 (S1) (2009) 175–183, http://dx.doi.org/10.1007/s12217-009-9151-7.

[25] V. Shevtsova, D.E. Melnikov, C.J. Legros, The post flight study of micro accelerations on-board of Russian spacecraft FOTON-12, 2002, URL https://www.researchgate.net/publication/236024379_The_Post_Flight_Study_of_Microacceleration_The_Post_Flight_Study_of_Micro_Accelerations_On-Board_of_Russian_Spacecraft_FOTON-12.

[26] R. Raj, J. Kim, J. McQuillen, Pool boiling heat transfer on the international space station: Experimental results and model verification, J. Heat Transfer 134 (10) (2012) http://dx.doi.org/10.1115/1.4006846.

[27] G.R. Warrier, V.K. Dhir, D.F. Chao, Nucleate pool boiling eXperiment (NPBX) in microgravity: International Space Station, Int. J. Heat Mass Transfer 83 (2015) 781–798, http://dx.doi.org/10.1016/j.ijheatmasstransfer.2014.12.054.

[28] K. Inoue, H. Ohta, Y. Toyoshima, H. Asano, O. Kawanami, R. Imai, K. Suzuki, Y. Shinmoto, S. Matsumoto, Heat loss analysis of flow boiling experiments onboard International Space Station with unclear thermal environmental conditions (1st report: Subcooled liquid flow conditions at test section inlet), Microgravity Sci. Technol. 33 (2) (2021) http://dx.doi.org/10.1007/s12217-021-09869-5.

[29] V.A. Thomas, N.S. Prasad, C.A.M. Reddy, Microgravity research platforms - A study, Current Sciences 79 (3) (2000) 336–340.

[30] N. Sentse, ESA user guide to low gravity platforms, 2014, URL https://www.esa.int/Science_Exploration/Human_and_Robotic_Exploration/Research/European_user_guide_to_low_gravity_platforms.

[31] I. Nejati, A. Sielaff, B. Franz, M. Zimmermann, P. Hänichen, K. Schweikert, J. Krempel, P. Stephan, A. Martin, H. Scheerer, T. Engler, M. Oechsner, Experimental investigation of single bubble nucleate boiling in microgravity, Microgravity Sci. Technol. (2020) http://dx.doi.org/10.1007/s12217-020-09813-z, 1875–0494.

[32] C. Harris, M. Stephens, A combined corner and edge detector, in: C.J. Taylor (Ed.), Procedings of the Alvey Vision Conference 1988, Alvey Vision Club, 1988, pp. 23.1–23.6, http://dx.doi.org/10.5244/C.2.23.

[33] J. Canny, A computational approach to edge detection, IEEE Trans. Pattern Anal. Mach. Intell. PAMI-8 (6) (1986) 679–698, http://dx.doi.org/10.1109/TPAMI.1986.4767851.

[34] M. Lebon, J. Sebilleau, C. Colin, Dynamics of growth and detachment of an isolated bubble on an inclined surface, Phys. Rev. Fluids 3 (7) (2018) http://dx.doi.org/10.1103/PhysRevFluids.3.073602.

[35] M.S. Plesset, S.A. Zwick, The growth of vapor bubbles in superheated liquids, J. Appl. Phys. 25 (4) (1954) 493–500, http://dx.doi.org/10.1063/1.1721668.

[36] B.B. Mikic, W.M. Rohsenow, P. Griffith, On bubble growth rates, Int. J. Heat Mass Transfer 13 (4) (1970) 657–666, http://dx.doi.org/10.1016/0017-9310(70)90040-2.

[37] G. Duhar, G. Riboux, C. Colin, Vapour bubble growth and detachment at the wall of shear flow, Heat Mass Transf. 45 (7) (2009) 847–855, http://dx.doi.org/10.1007/s00231-007-0287-y.

[38] M.J. Prince, H.W. Blanch, Bubble coalescence and break-up in air-sparged bubble columns, AIChE J. 36 (10) (1990) 1485–1499, http://dx.doi.org/10.1002/aic.690361004.

[39] C. Colin, X. Riou, J. Fabre, Bubble coalescence in gas–liquid flow at microgravity conditions, Microgravity Sci. Technol. 20 (3–4) (2008) 243–246, http://dx.doi.org/10.1007/s12217-008-9031-6.

[40] H.S. Abarajith, V.K. Dhir, G. Warrier, G. Son, Numerical simulation and experimental validation of the dynamics of multiple bubble merger during pool boiling under microgravity conditions, Ann. New York Acad. Sci. 1027 (1) (2004) 235–258, http://dx.doi.org/10.1196/annals.1324.020.

[41] I. Golobic, J. Petkovsek, D.B.R. Kenning, Bubble growth and horizontal coalescence in saturated pool boiling on a titanium foil, investigated by high-speed IR thermography, Int. J. Heat Mass Transfer 55 (4) (2012) 1385–1402, http://dx.doi.org/10.1016/j.ijheatmasstransfer.2011.08.021.

[42] T. Chen, J.N. Chung, Coalescence of bubbles in nucleate boiling on microheaters, Int. J. Heat Mass Transfer 45 (11) (2002) 2329–2341, http://dx.doi.org/10.1016/S0017-9310(01)00334-9.

[43] T. Chen, J.N. Chung, Heat-transfer effects of coalescence of bubbles from various site distributions, Proc. R. Soc. Lond. Ser. A Math. Phys. Eng. Sci. 459 (2038) (2003) 2497–2527, http://dx.doi.org/10.1098/rspa.2003.1133.

[44] A. Coulibaly, J. Bi, D.M. Christopher, Experimental investigation of bubble coalescence heat transfer during nucleate pool boiling, Exp. Therm Fluid Sci. 104 (2019) 67–75, http://dx.doi.org/10.1016/j.expthermflusci.2019.01.024.

[45] Q. Kang, H.L. Cui, L. Hu, L. Duan, W.R. Hu, Experimental investigation on bubble coalescence under nonuniform temperature distribution in reduced gravity, J. Colloid Interface Sci. 310 (2) (2007) 546–549, http://dx.doi.org/10.1016/j.jcis.2007.02.020.

[46] J. Kim, Review of nucleate pool boiling bubble heat transfer mechanisms, Int. J. Multiph. Flow. 35 (12) (2009) 1067–1076, http://dx.doi.org/10.1016/j.ijmultiphaseflow.2009.07.008.

[47] G. Saccone, A.I. Garivalis, P. Di Marco, Electrohydrodynamics and boiling: Experiments, numerical calculation and modeling of Maxwell stress tensor and electric force acting on bubbles, J. Electrost. 103 (2020) 103413, http://dx.doi.org/10.1016/j.elstat.2019.103413.

[48] P. Di Marco, R. Kurimoto, G. Saccone, K. Hayashi, A. Tomiyama, Bubble shape under the action of electric forces, Exp. Therm Fluid Sci. 49 (2013) 160–168, http://dx.doi.org/10.1016/j.expthermflusci.2013.04.015.

[49] P. Di Marco, The use of electric force as a replacement of buoyancy in two-phase flow, Microgravity Sci. Technol. 24 (3) (2012) 215–228, http://dx.doi.org/10.1007/s12217-012-9312-y.